

Modular multiscale approach to modelling high-harmonic generation in gases

Jan Vábek^{a,b}, Tadeáš Němec^{a,b}, Stefan Skupin^c, Fabrice Catoire^d

^a*ELI Beamlines Facility, The Extreme Light Infrastructure ERIC, Za Radnicí 835, Dolní Břežany, 25241, Czech Republic,*

^b*Czech Technical University in Prague, Faculty of Nuclear Sciences and Physical Engineering, Břehová 7, Prague 1, 11519, Czech Republic,*

^c*Université Claude Bernard Lyon 1, CNRS, Institut Lumière Matière, UMR5306, Villeurbanne, F-69100, France,*

^d*Centre Lasers Intenses et Applications, Université de Bordeaux-CNRS-CEA, Talence Cedex, 33405, France,*

Abstract

We present a modular user-oriented simulation toolbox for studying high-harmonic generation in gases [1]. The first release consists of the computational pipeline to 1) compute the unidirectional IR-pulse propagation in cylindrical symmetry, 2) solve the microscopic responses in the whole macroscopic volume using a 1D-TDSE solver, 3) obtain the far-field harmonic field using a diffraction-integral approach. The code comes with interfaces and tutorials, based on practical laboratory conditions, to facilitate the usage and deployment of the code both locally and in HPC-clusters. Additionally, the modules are designed to work as stand-alone applications as well, e.g., 1D-TDSE is available through Pythonic interface.

1. Introduction

This code package originates from a joint effort of the high harmonic generation (HHG) and ultrashort-filament communities. It couples 1) a code originally designed for studying the reshaping and filaments due to the non-linear laser pulse propagation and 2) codes for solving the time-dependent Schrödinger equation (TDSE) and linear XUV-field propagation used for modelling HHG. The outcome of this effort is a modular computational toolbox, which allows for modelling HHG experiments including both macroscopic and microscopic aspects of the problem. The modules presented in

this first release limit the modelling to linear polarisation and cylindrical symmetry of the propagation. The main goal is to provide a full model for one-to-one correspondence to laboratory HHG experiments; however, the different modules of the code are designed to be used as stand-alone applications to address various problems related to HHG independently. Before we proceed to the code itself, we review the physical context.

High harmonic generation (HHG) in a gaseous medium is a source of coherent XUV radiation arising from a highly non-linear response of the medium induced by an IR driving laser pulse [2, 3, 4, 5, 6]. Because other non-linear effects, such as plasma defocusing, are also present, the driving pulse undergoes strong reshaping. The fundamental physical origin of HHG lies in the interaction of a single atom with the external field, which is captured by the well-known three-step model and rigorously described by solving the time-dependent Schrödinger equation. The IR-to-XUV conversion efficiency is low, posing challenges for applications that require high-intensity XUV pulses, such as XUV–XUV pump–probe experiments. From a computational perspective, the limited XUV intensity simplifies the modelling, as the XUV field does not exhibit significant self-induced non-linear reshaping.

Historically, our model is a result of evolution of different codes used in the aforementioned areas. The HHG codes were used for phenomena where the macroscopic aspect did not need to be taken into account or the driving field was simple [7, 8, 9]. Finally, the full coupling of the code was shown [10].

To sort it out, our modular solution provides a separate code for each of the subproblems:

1. The non-linear laser propagation is computed under the cylindrical symmetry by CUPRAD. As this is the first code in the chain, it can be easily run independently;
2. The microscopic response is retrieved from a numerical solution of TDSE. The code is compiled into an MPI application and a dynamic library, which can be accessed directly from Python;
3. The XUV propagation is retrieved from a diffraction integral. It is implemented as a Pythonic module, which can be easily fed by any user-defined microscopic dipoles;

and all the modules can be pipelined together to provide a comprehensive multiscale picture of HHG. The communication channel between the modules is the interface by data relying in the HDF5 data format, which also ensures the completeness as all the inputs and outputs can be packed together. It also

ensures easy processing and manipulation of data. The whole computation forms a pipeline, which can be executed at once.

This paper serves as the top layer of documentation: it discusses the physical background and the used computational methods (Section 2 for CUPRAD, Section 3 for HHG, Section 4 for the implementations of all the models), interfaces (Section 5), the usage of the Pythonic CTDSE library (Section 6), and shows some examples how to use it (Section 7). Alongside the paper, there are documentations of the respective modules directly in the *git repository* [1]. This repository also includes jupyter notebooks with showcases of the code (see also Section 7, which presents these results in this manuscript). The key parts of the model are documented directly in the code for fine details about the concrete computational routines. The repository also contains guidelines to use the code within a docker container and how to install it on HPC clusters.

Throughout the work, we use \hat{f} to denote the time Fourier transform of f . The description of the whole physics is done in SI units except the microscopic physics (Sections 3.1, 4.2 and 6).

2. Infrared Propagation

In this section, we provide the model equations for describing the propagation of ultrashort ionizing pulses in gases. For the present purposes and the parameter ranges envisaged, a *complex envelope description* of the scalar optical field by an extended nonlinear Schrödinger equation in cylindrical coordinates is sufficient [11, 12]. The derivation formulates the propagation in the terms of the complex envelope, it exploits the slowly varying envelope approximation (SVEA) in space and time, accounting possibility of higher-order corrections like space-time coupling and self-steepening [13]. In a future update, the code will be extended to the unidirectional pulse propagation equation [14], which is not based on SVEA and allows the description of e.g. few-cycle pulses. The restriction to linearly polarized (scalar) fields and cylindrical geometries will also be lifted in the future. In the following, we briefly outline the derivation of the propagation models implemented in the current version of CUPRAD.

Starting point are macroscopic Maxwell's equations

$$\nabla \cdot \mathbf{E}(\mathbf{r}, t) = \frac{\rho(\mathbf{r}, t) - \nabla \cdot \mathbf{P}(\mathbf{r}, t)}{\epsilon_0} \quad (1a)$$

$$\nabla \cdot \mathbf{B}(\mathbf{r}, t) = 0 \quad (1b)$$

$$\nabla \times \mathbf{E}(\mathbf{r}, t) = -\frac{\partial}{\partial t} \mathbf{B}(\mathbf{r}, t) \quad (1c)$$

$$\nabla \times \mathbf{H}(\mathbf{r}, t) = \mathbf{J}(\mathbf{r}, t) + \epsilon_0 \frac{\partial}{\partial t} \mathbf{E}(\mathbf{r}, t) + \frac{\partial}{\partial t} \mathbf{P}(\mathbf{r}, t), \quad (1d)$$

where all fields involved, namely the electric field \mathbf{E} , the polarization vector \mathbf{P} , the magnetic field \mathbf{H} , the magnetic induction vector \mathbf{B} , the carrier density ρ and the current density \mathbf{J} , are real valued.

Gases are isotropic, non-magnetizable media with a nonlinear polarization vector. Moreover, the spectral range of the laser field should be far from any material resonances. Thus we can use the conventional description of nonlinear optics, and express \mathbf{P} as a power series in \mathbf{E} :

$$\widehat{\mathbf{P}}(\mathbf{r}, \omega) = \widehat{\mathbf{P}}^{(1)}(\mathbf{r}, \omega) + \widehat{\mathbf{P}}^{(3)}(\mathbf{r}, \omega) + \widehat{\mathbf{P}}^{(5)}(\mathbf{r}, \omega) + \widehat{\mathbf{P}}^{(7)}(\mathbf{r}, \omega) + \dots \quad (2a)$$

$$\widehat{P}_\mu^{(j)}(\mathbf{r}, \omega) = \epsilon_0 \sum_{\alpha_1 \dots \alpha_j} \int \dots \int \chi_{\mu\alpha_1 \dots \alpha_j}^{(j)}(\mathbf{r}, -\omega_\sigma; \omega_1, \dots, \omega_j) \quad (2b)$$

$$\times \widehat{E}_{\alpha_1}(\mathbf{r}, \omega_1) \dots \widehat{E}_{\alpha_j}(\mathbf{r}, \omega_j) \delta(\omega - \omega_\sigma) d\omega_1 \dots d\omega_j$$

$$\omega_\sigma = \omega_1 + \dots + \omega_j. \quad (2c)$$

For the magnetic induction we have

$$\widehat{\mathbf{B}}(\mathbf{r}, \omega) = \mu_0 \widehat{\mathbf{H}}(\mathbf{r}, \omega). \quad (3)$$

For technical convenience, we express these relations in Fourier space, and the corresponding transformations are defined as

$$\widehat{\mathbf{F}}(\mathbf{r}, \omega) = \frac{1}{2\pi} \int \mathbf{F}(\mathbf{r}, t) e^{i\omega t} dt \quad (4)$$

$$\mathbf{F}(\mathbf{r}, t) = \int \widehat{\mathbf{F}}(\mathbf{r}, \omega) e^{-i\omega t} d\omega. \quad (5)$$

In Equation (2a) we take into account the fact that in isotropic media all susceptibility tensors $\overset{\leftrightarrow}{\chi}^{(j)}$, j even, vanish due to spatial symmetry relations [15].

The subscripts $\mu, \alpha_1, \dots, \alpha_j$ in Equation (2b) indicate the respective field vector component in Cartesian coordinates. As indicated by the summation sign, $\alpha_1, \dots, \alpha_j$ are to be summed over $x, y,$ and z . In the following, we specify Equation (2a) for the media under consideration. We shall see later that for the field intensities under consideration $|\mathbf{P}^{(3)}| \ll |\mathbf{P}^{(1)}|$ is already justified, thus in the expansion (2a) we neglect terms of order higher than three¹.

The linear polarization $\widehat{\mathbf{P}}^{(1)}$ can be further simplified. In isotropic media the tensor $\overset{\leftrightarrow}{\chi}^{(1)}$ is diagonal and only a single independent element remains: $\chi_{\mu\alpha}^{(1)} = \chi_{xx}^{(1)}\delta_{\mu\alpha}$. Hence, with the convention $\chi^{(1)}(\mathbf{r}, \omega) = \chi_{xx}^{(1)}(\mathbf{r}, -\omega; \omega)$, we have

$$\widehat{\mathbf{P}}^{(1)}(\mathbf{r}, \omega) = \epsilon_0 \chi^{(1)}(\mathbf{r}, \omega) \widehat{\mathbf{E}}(\mathbf{r}, \omega), \quad (6)$$

and we define the scalar dielectric function

$$\epsilon(\mathbf{r}, \omega) = 1 + \chi^{(1)}(\mathbf{r}, \omega). \quad (7)$$

The third order nonlinear polarization $\widehat{\mathbf{P}}^{(3)}$ is determined by the 81 components of the general fourth-rank tensor $\overset{\leftrightarrow}{\chi}^{(3)}$. Again we benefit from the isotropy of the medium and from spatial symmetry relations [15] it is possible to show

$$\chi_{\mu\alpha_1\alpha_2\alpha_3}^{(3)} = \chi_{xxyy}^{(3)}\delta_{\mu\alpha_1}\delta_{\alpha_2\alpha_3} + \chi_{xyyx}^{(3)}\delta_{\mu\alpha_3}\delta_{\alpha_1\alpha_2} + \chi_{xyxy}^{(3)}\delta_{\mu\alpha_2}\delta_{\alpha_1\alpha_3}. \quad (8)$$

Moreover, we consider media with homogeneous nonlinearity and quasi linearly polarized electric fields $\mathbf{E} = E_x \mathbf{e}_x$ only. Therefore, only one relevant component of the tensor remains and with the definition

$$\chi^{(3)} = \chi_{xxxx}^{(3)} = \chi_{xxyy}^{(3)} + \chi_{xyyx}^{(3)} + \chi_{xyxy}^{(3)} \quad (9)$$

we have

$$\begin{aligned} \widehat{\mathbf{P}}^{(3)}(\mathbf{r}, \omega) &= \mathbf{e}_x \epsilon_0 \iint \chi^{(3)}(\omega; \omega_1, \omega_2, \omega - \omega_1 - \omega_2) \\ &\quad \times \widehat{E}_x(\mathbf{r}, \omega_1) \widehat{E}_x(\mathbf{r}, \omega_2) \widehat{E}_x(\mathbf{r}, \omega - \omega_1 - \omega_2) d\omega_1 d\omega_2. \end{aligned} \quad (10)$$

As expected, in an isotropic medium the nonlinear polarization vector is parallel to the electric field.

¹In CUPRAD it is possible to account for the fifth order nonlinearity as well. However, for conciseness, we do not include it in the present derivation.

In media of interest, such as air or noble gases, $\epsilon(\omega)$ is real valued and positive for wavelengths ranging from infrared to ultraviolet. The linear refractive index is defined by $n(\omega) = \sqrt{\epsilon(\omega)}$ and the wavenumber by $k(\omega) = \omega n(\omega)/c$. We are interested in the propagation of a quasi-linear polarized pulsed beam, whose spectrum is centered around the operating frequency ω_0 . Assuming a sufficiently small spectral bandwidth $\Delta\omega$, we can expand $k(\omega)$ in a Taylor series around ω_0

$$k(\omega) = k_0 + k'\bar{\omega} + \frac{1}{2}k''\bar{\omega}^2 + \frac{1}{6}k'''\bar{\omega}^3 + \dots \quad (11a)$$

$$k^2(\omega) = k_0^2 + 2k_0k'\bar{\omega} + k'^2\bar{\omega}^2 + k_0k''\bar{\omega}^2 + k'k''\bar{\omega}^3 + \frac{k_0k'''}{3}\bar{\omega}^3 + \dots, \quad (11b)$$

where $\bar{\omega} = \omega - \omega_0$. The complex slowly varying envelope function \mathcal{E} of the electric field \mathbf{E} is defined by

$$\mathbf{E}(\mathbf{r}, t) = \sqrt{\frac{\omega_0\mu_0}{2k_0}} \mathcal{E}(x, y, z, t) e^{i(k_0z - \omega_0t)} + \text{c.c.} \quad (12)$$

The x -component of the optical field is assumed to be the dominant one, $|\mathcal{E}_x| \gg |\mathcal{E}_{y,z}|$, and we write $\mathcal{E} = \mathcal{E}_x$. The field envelope \mathcal{E} is assumed to change slowly in $\alpha = x, y, z$ and t

$$\left| \frac{\partial}{\partial \alpha} \mathcal{E} \right| \ll k_0 |\mathcal{E}| \quad (13a)$$

$$\left| \frac{\partial}{\partial t} \mathcal{E} \right| \ll \omega_0 |\mathcal{E}|. \quad (13b)$$

This is justified if the field envelope \mathcal{E} does not change on length scales comparable to the wavelength $\lambda = 2\pi/k_0$ and on time scales comparable to the optical cycle $T_{cyc} = 2\pi/\omega_0$.

Strictly speaking, the computation of the third-order nonlinear polarization vector $\mathbf{P}^{(3)}$ for pulses requires knowing the frequency dependencies of the nonlinear susceptibility over the relevant part of the spectrum [see Eq. (10)]. However, this is generally not necessary when the laser frequency is far from material resonances. Here, we will use a common approximation for the third-order nonlinearity in gases reading

$$\mathbf{P}^{(3)}(t) = \epsilon_0 \sqrt{\frac{\omega_0\mu_0}{2k_0}} 2n_b n_2 \int \mathcal{R}(t-t') |\mathcal{E}(t')|^2 dt' \mathcal{E}(t) e^{i(k_0z - \omega_0t)} + \text{c.c.} \quad (14a)$$

$$\mathcal{R}(t) = (1 - x_{dK}) \delta(t) + x_{dK} \frac{1 + \Omega^2 \tau_K^2}{\Omega \tau_K^2} \Theta(t) e^{-\frac{t}{\tau_K}} \sin(\Omega t), \quad (14b)$$

where δ denotes the Dirac δ -distribution and Θ the Heaviside function. In this intensity-dependent nonlinear polarization, often called Kerr response, we neglect third-harmonic generation due to the large phase mismatch $\Delta k = 3k_0 - k(3\omega_0)$ (e.g. $\Delta k = -5 \text{ cm}^{-1}$ @ 800 nm in air). The Kerr response of noble gases is instantaneous ($x_{dK} = 0$), but for air or other molecular gases, a delayed contribution $\sim \exp(-t/\tau_K)$ appears with a ratio of x_{dK} . The instantaneous part $\sim \delta(t)$ describes the response that comes from the bound electrons. Electronic response times are about a few femtoseconds or less and therefore considerably shorter than the duration of the pulse envelopes under consideration. The delayed part $\sim \exp(-t/\tau_K)$ accounts for the nuclear response, namely the ro-vibrational Raman contribution. The delay time τ_K and the inverse resonance frequency $1/\Omega$ are in the same range as the pulse lengths of ~ 100 fs considered.

As mentioned before, high intensities require the modeling of both ionization of gas atoms or molecules and feedback of the generated charge carriers to the laser field. Depending on the gas and the intensity range, different photo-ionization models can be used, e.g., a simple multi-photon ionization rate or the more general Perelomov-Popov-Terent'ev theory [16], to name a few. All of these models yield a cycle-averaged, intensity-dependent photo-ionization rate $\mathcal{W}_{PI}(I)$, which drives the temporal evolution of the electron density ρ_e . In the course of the derivation we will see that for consistency we have to take into account a second ionization mechanism, the avalanche ionization by free electrons accelerated by the laser field. In gases, this mechanism is usually much weaker than photo-ionization. The complete equation for the evolution of the electron density ρ_e thus reads

$$\frac{\partial}{\partial t} \rho_e(\mathbf{r}, t) = [\mathcal{W}_{PI}(I) + \mathcal{W}_{AI}(I, \rho_e)] \rho_{nt}(\mathbf{r}, t), \quad (15)$$

where \mathcal{W}_{AI} is the avalanche ionization rate, and ρ_{nt} is the neutral density². Here, $\rho_{nt} = \rho_{nt}^0 - \rho_e$ is not constant in time, but accounts for the depletion of neutrals by ionization. We neglect diffusion of carriers because this process acts on time scales ≥ 1 ps. Hence, they are too slow to influence femtosecond pulses. It is worth noticing that in the framework of the present derivation, the electron density ρ_e is also a slowly varying entity, such as \mathcal{E} .

²In CUPRAD it is possible to account for recombination as well. However, for conciseness, we do not include it in the present derivation.

Oscillations of the free electrons driven by the electric field are taken into account by a Drude model. We assume a free electron gas on a positive background. This background is provided by the ions and the total carrier density $\rho = 0$ vanishes. Because the mass of the ions is ~ 30000 times the electron mass, we neglect ion motions and, therefore, their contribution to the current density. Then the free electron current density $\mathbf{J}_e(\mathbf{r}, t)$ is governed by

$$\frac{\partial}{\partial t} \mathbf{J}_e + \frac{1}{\tau_0} \mathbf{J}_e = \frac{q_e^2}{m_e} \rho_e \mathbf{E}. \quad (16)$$

Here q_e accounts for the electron charge, τ_0 is the electron collision time, and m_e the electron mass. The motion of free electrons is dominated by the fast oscillations of the linear polarized optical field at ω_0 , and it is justified to introduce a complex slowly varying envelope \mathcal{J}_e ,

$$\mathbf{J}_e(\mathbf{r}, t) = \sqrt{\frac{\omega_0 \mu_0}{2k_0}} \mathcal{J}_e(x, y, z, t) e^{i(k_0 z - \omega_0 t)} + \text{c.c.}, \quad (17)$$

analogous to Equation (12). We can solve Equation (16) formally as

$$\mathcal{J}_e = \frac{q_e^2}{m_e \omega_0} \left(-i\hat{T} + \frac{1}{\tau_0 \omega_0} \right)^{-1} \rho_e \mathcal{E}, \quad (18)$$

where $\hat{T} = 1 + \mathbf{i}\partial_t/\omega_0$. A slowly varying envelope condition such as (13b) can be formulated for the product $\rho_e \mathcal{J}_e$ and reads $|\partial_t \rho_e \mathcal{E}|/\omega_0 \ll |\rho_e \mathcal{E}|$. Thus, together with $1/\tau_0 \omega_0 \ll 1$, it is justified to simplify Equation (18) to

$$\mathcal{J}_e = \frac{q_e^2}{m_e \omega_0} \left(\frac{1}{\tau_0 \omega_0} + \mathbf{i}\hat{T}^{-1} \right) \rho_e \mathcal{E}, \quad (19)$$

which is much more convenient for the following derivation.

As in the case of the ionization rates, it turns out that, for consistency, we have to consider a second contribution to the current density: The generation of free carriers by photo-ionization. Because this term will lead to a loss current in our final equations, we call it \mathbf{J}_{IL} and

$$\mathbf{J}(\mathbf{r}, t) = \mathbf{J}_e(\mathbf{r}, t) + \mathbf{J}_{IL}(\mathbf{r}, t). \quad (20)$$

The corresponding complex slowly varying envelopes \mathcal{J} and \mathcal{J}_{IL} are defined as the analogues of \mathcal{J}_e , cf. Eq. (17)].

Using the energy conservation law, it is possible to derive self-consistent expressions for \mathcal{W}_{AI} and \mathcal{J}_{IL} . On the one hand, the temporal evolution of the local energy density w in the medium is determined by

$$\frac{d}{dt}w(\mathbf{r}, t) = \mathbf{J}(\mathbf{r}, t) \cdot \mathbf{E}(\mathbf{r}, t). \quad (21)$$

Hence, we can compute the energy transferred to the medium by the pulse at the position \mathbf{r} in a small volume $\Delta V = \lambda_0^3$ by

$$\begin{aligned} W_{\Delta V}(\mathbf{r}) &= \int_0^{\lambda_0} \int_0^{\lambda_0} \int_0^{\lambda_0} \int_{-\infty}^{\infty} \mathbf{J}(\mathbf{r} + \mathbf{r}', t) \cdot \mathbf{E}(\mathbf{r} + \mathbf{r}', t) dt d^3r' \\ &= \lambda_0^3 \int \frac{\mu_0 q_e^2}{m_e \tau_0 \omega_0 k_0} \rho_e(\mathbf{r}, t) |\mathcal{E}(\mathbf{r}, t)|^2 + \frac{\omega_0 \mu_0}{2k_0} [\mathcal{J}_{IL}(\mathbf{r}, t) \cdot \mathcal{E}^*(\mathbf{r}, t) + \text{c.c.}] dt. \end{aligned} \quad (22)$$

Note that terms containing $\mathbf{i}T^{-1}$ cancel via integration by parts and that fast oscillating terms proportional to $\exp[\pm \mathbf{i}2(k_0 z - \omega_0 t)]$ do not contribute to the integral. Moreover, the choice of ΔV is arbitrary, its dimensions just have to be large against the scales of the electron movement and small compared to the length scales of the slowly varying envelopes.

On the other hand, we know that energy transferred to the medium by the optical field causes ionization of neutral atoms or molecules of the gas. We assume that all energy losses due to collisions [term $\sim 1/\tau_0$ in Equation (16)] contribute to avalanche ionization. Hence we have

$$W_{\Delta V}(\mathbf{r}) = \lambda_0^3 U_i \int [\mathcal{W}_{PI}(I) + \mathcal{W}_{AI}(I, \rho_e)] \rho_{nt}(\mathbf{r}, t) dt, \quad (23)$$

where U_i is the ionization energy of the atoms or molecules. The term $\propto \mathcal{W}_{PI}$ gives the energy consumption of photo-ionization, and the term $\propto \mathcal{W}_{PA}$ the energy consumption of avalanche ionization. In terms of the slowly varying envelopes, the energy transfer is local and instantaneous. Both ionization processes act on time scales comparable to the oscillation of the carrier wave or less, and the motion of the free electrons takes place on nanometer scales. Therefore, it is justified to omit the time integral when we equate the expressions of Equations (22) and (23):

$$\frac{\mu_0 q_e^2}{m_e \tau_0 \omega_0 k_0} \rho_e |\mathcal{E}|^2 + \frac{\omega_0 \mu_0}{k_0} \text{Re}(\mathcal{J}_{IL} \cdot \mathcal{E}^*) = U_i \mathcal{W}_{PI} \rho_{nt} + U_i \mathcal{W}_{AI} \rho_{nt}. \quad (24)$$

We claim above that we can derive \mathcal{W}_{AI} and \mathbf{J}_{IL} self-consistently. In fact, Equation (24) links both \mathcal{W}_{AI} and \mathbf{J}_{IL} to known quantities. However, additional arguments are necessary to make them unique. First, we assume that \mathbf{J}_{IL} causes energy losses only, e.g., $\text{Im}(\mathbf{J}_{IL} \cdot \mathcal{E}^*) = 0$. This is a rather formal constraint, because there is no physical argument that ionization should influence the optical field other than by losses. Second, we assume that the current density \mathbf{J}_{IL} is caused by photo-ionization only, and that \mathbf{J}_{IL} is parallel to \mathbf{E} . With these additional assumptions, Equation (24) leads to

$$\mathbf{J}_{IL} = \frac{k_0}{\omega_0 \mu_0} U_i \frac{\mathcal{W}_{PI}}{|\mathcal{E}|^2} \rho_{nt} \mathcal{E}, \quad (25)$$

and with $\sigma = \mu_0 q_e^2 / m_e \tau_0 \omega_0 k_0$

$$\mathcal{W}_{AI} = \frac{\sigma}{U_i \rho_{nt}} \rho_e |\mathcal{E}|^2. \quad (26)$$

We proceed and justify that we can neglect $\nabla \cdot \mathbf{E}$ in the derivation of the wave equation. Under the present assumptions, Equation (1a) reads

$$\nabla \cdot \mathbf{E} = -\frac{\nabla \cdot \mathbf{P}^{(3)}}{\epsilon_0 \epsilon}, \quad (27)$$

and we want to show that $|\nabla \cdot \mathbf{E}| \ll |\partial_x E_x|$. Despite its complicated expression, the magnitude of the nonlinear polarization is $\sim 2\epsilon_0 n_b n_2 I \mathbf{E}$, and for the gases and intensity ranges under consideration $|n_2 I| \ll n_b = n(\omega_0)$ holds. After some algebra and using (13a) one can show that $|\nabla \cdot \mathbf{P}^{(3)}| / \epsilon_0 \epsilon \ll |\partial_x E_x|$. Hence, $\nabla \cdot \mathbf{E} = 0$ is justified and we are able to derive the wave equation

$$\Delta \mathbf{E} - \frac{1}{c^2} \frac{\partial^2}{\partial t^2} \mathbf{E} = \mu_0 \left(\frac{\partial^2}{\partial t^2} \mathbf{P} + \frac{\partial}{\partial t} \mathbf{J} \right). \quad (28)$$

With the slowly varying envelopes and the expressions for polarization [Equations (2a), (6), and (14)] and current density [Equations (19), (20), and (25)] derived above we get

$$\begin{aligned} & \left(\frac{\partial}{\partial z} + \mathbf{i}k_0 \right)^2 \mathcal{E} + \Delta_{\perp} \mathcal{E} + \int k^2 (\omega_0 + \bar{\omega}) \hat{\mathcal{E}}(\mathbf{r}, \bar{\omega}) e^{-\mathbf{i}\bar{\omega}t} d\bar{\omega} \\ &= -\frac{2k_0^2 n_2}{n_b} \hat{T}^2 \int \mathcal{R}(t-t') |\mathcal{E}(t')|^2 dt' \mathcal{E} + \frac{k_0^2}{n_b^2 \rho_c} \rho_e \mathcal{E} \\ & \quad - \mathbf{i}k_0 \hat{T} \left(\sigma \rho_e \mathcal{E} + U_i \frac{\mathcal{W}_{PI}}{|\mathcal{E}|^2} \rho_{nt} \mathcal{E} \right), \end{aligned} \quad (29)$$

where $\rho_c = m_e \epsilon_0 \omega_0^2 / q_e^2$ is the critical plasma density.

Our goal is to model the evolution of short laser pulses propagating in gaseous media such as noble gases and air. These pulses are traveling at a certain velocity in the z -direction. In the linear regime, they travel at the group velocity $v_g(\omega_0) = 1/k'$, and it is a good assumption that the nonlinear effects under consideration will not change this too much. Hence, the derivation of the field envelope \mathcal{E} with respect to z is dominated by the motion of the pulse, and we have

$$\left| \frac{\partial}{\partial z} \mathcal{E} + k' \frac{\partial}{\partial t} \mathcal{E} \right| \ll \left| \frac{\partial}{\partial z} \mathcal{E} \right|. \quad (30)$$

Hence, with the transformation into coordinates moving with the pulse, $\tilde{t} = t - k'z$ and $\tilde{z} = z$, it is possible to achieve an even weaker dependency of the field envelope on the propagation variable. With Eqs. (13) and (30) we see

$$\left| \frac{\partial}{\partial \tilde{z}} \mathcal{E} \right| = |\partial_z \mathcal{E} + k' \partial_t \mathcal{E}| \ll \left| \frac{\partial}{\partial z} \mathcal{E} \right| \ll k_0 |\mathcal{E}|. \quad (31)$$

For simplicity, we will remove the tilde \sim after applying the transformation, and with Equation (11b) the left-hand side of Eq. (29) reads

$$\frac{\partial}{\partial z} \left(1 + \mathbf{i} \frac{k'}{k_0} \frac{\partial}{\partial t} - \frac{\mathbf{i}}{2k_0} \frac{\partial}{\partial z} \right) \mathcal{E} - \frac{\mathbf{i} \Delta_{\perp} \mathcal{E}}{2k_0} + \frac{\mathbf{i} k''}{2} \left(1 + \mathbf{i} \frac{k'}{k_0} \frac{\partial}{\partial t} + \frac{\mathbf{i}}{3} \frac{k'''}{k''} \frac{\partial}{\partial t} \right) \frac{\partial^2 \mathcal{E}}{\partial t^2}. \quad (32)$$

In gases, it is justified to assume $k' = 1/c$, $n_b = 1$ and therefore $1 + \mathbf{i} k' \partial_t / k_0 = \hat{T}$. With the relation (31) we neglect in (32) the second derivative with respect to z , and after multiplying with the inverse operator \hat{T}^{-1} the ultimate propagation equation reads

$$\begin{aligned} & \frac{\partial}{\partial z} \mathcal{E} - \frac{\mathbf{i}}{2k_0} \hat{T}^{-1} \Delta_{\perp} \mathcal{E} + \mathbf{i} \frac{k''}{2} \frac{\partial^2}{\partial t^2} \mathcal{E} - \frac{k'''}{6} \frac{\partial^3}{\partial t^3} \mathcal{E} \\ & = \mathbf{i} k_0 n_2 \hat{T} \int \mathcal{R}(t - t') |\mathcal{E}(t')|^2 dt' \mathcal{E} - \mathbf{i} \frac{k_0}{2\rho_c} \hat{T}^{-1} \rho_e \mathcal{E} - \frac{\sigma}{2} \rho_e \mathcal{E} - U_i \frac{\mathcal{W}_{PI}}{2 |\mathcal{E}|^2} \rho_{nt} \mathcal{E}. \end{aligned} \quad (33)$$

It is interesting to note that Equation (33) takes into account all deviations from unity of the order $|\partial_t \mathcal{E}| / \omega_0$ and therefore goes beyond the ordinary

slowly varying envelope approximation [13],

$$\begin{aligned} & \frac{\partial}{\partial z} \mathcal{E} - \mathbf{i} \frac{1}{2k_0} \Delta_{\perp} \mathcal{E} + \mathbf{i} \frac{k''}{2} \frac{\partial^2}{\partial t^2} \mathcal{E} \\ &= \mathbf{i} k_0 n_2 \int \mathcal{R}(t-t') |\mathcal{E}(t')|^2 dt' \mathcal{E} - \mathbf{i} \frac{k_0}{2\rho_c} \rho_e \mathcal{E} - \frac{\sigma}{2} \rho_e \mathcal{E} - U_i \frac{\mathcal{W}_{PI}}{2|\mathcal{E}|^2} \rho_{nt} \mathcal{E}. \end{aligned} \quad (34)$$

In CUPRAD, both Equations (33) and (34) are implemented, and one can switch between them by setting the variable `numerics_operators_t_t-1`. As already mentioned in the introduction, CUPRAD assumes cylindrical coordinates ρ, z, t with $\rho = \sqrt{x^2 + y^2}$.

3. High Harmonic Generation and Propagation

Here we present the physical model of the HHG part, which consists of two main tasks: 1) to compute all the microscopic source terms of the XUV radiation in all the points in the macroscopic volume; 2) to sum up all the microscopic emitters to obtain the macroscopic XUV signal.

The high-harmonic generation in gases is a non-relativistic process because too high intensity is preventing the generation [4]. A quantum-mechanical approach is necessary for an accurate description as the generation process involves the interaction of electronic wavepacket with the atomic shells. A suitable model is then the Schrödinger equation, which is computed on a regular grid covering the interaction volume. Finally, all the emitters are integrated to obtain the far-field XUV signal. The details about the physical models used in our code are discussed in the following two subsections.

3.1. Microscopic Response in XUV regime (TDSE)

In this section we describe the solution of the interaction of a single atom with an external laser field, which is solved many times for all the points in the macroscopic volume defined by the laser field. Therefore, the microscopic response is solved at *a fixed macroscopic coordinate* and the spatial variable in this section is related only to the *microscopic system*. Full microscopic dynamics of the interest is encoded in the solution of the Schrödinger equation,

$$\mathbf{i} \frac{\partial}{\partial t} \psi(\mathbf{x}, t) = H(t) \psi(\mathbf{x}, t), \quad (35)$$

describing the interaction of an atom with an external laser field. (Note, we use the atomic units within this section.) A completely general solution will be a high-dimensional problem including all the electrons of the atom, with the electrons living in a large-dimensional Hilbert. We need to drastically reduce the dimensionality to make the problem manageable, while keeping the essential physical effects.

The current model supports only linearly polarized fields within the dipole approximation and treats only single active electron without spin, which allows to use one-dimensional geometry for TDSE. Generally, the incident laser field is defined by the scalar, $\phi(x, t)$, and vector, $A(x, t)$, potentials; and the Hamiltonian of an electron within the influence of the laser pulse and coulomb potential V_C reads $H = (p - A)^2/2 + V_C - \phi$. The potentials include gauge-freedom, which does not affect the electric field $E = -\frac{\partial}{\partial t}A - \frac{\partial}{\partial x}\phi$.

Our solver is implemented in the length-gauge, which allows to efficiently use directly the outputs of CUPRAD, the Hamiltonian is

$$H(t) = -\frac{p^2}{2} + V_C - xE(t), \quad (36a)$$

$$V_C = -\frac{1}{\sqrt{x^2 + a^2}}, \quad (36b)$$

where the only free parameter a is chosen to match the ground-state energy E_g of the field-free Hamiltonian $H_0 = p^2/2 + V_C$. Note that including more parameters in the model potential allows to match closer the 3D-atomic model [17]. The implementation of these features together with other improvements such as the exterior complex scaling [18, 19] and optimised grid representation [20]; and finally the inclusion of a 3D-TDSE solver within the model. Regarding the gauge choice; although physics is gauge-invariant, it might be convenient to transform the gauge for some calculations. Namely, the velocity gauge ($\phi = 0$) is another choice popular in atomic physics. The gauge transformations of the results does not pose any difficulty as it means just multiplication by a phase factor, $\psi'(x, t) = e^{i\Lambda(x,t)}\psi(x, t)$, where Λ is the gauge-transformation function (see Chapter 6.3 of [21]).

The central quantity of the interest is the dipole acceleration, which reads (keeping the length gauge fixed):

$$\partial_t j_Q(x, t) = \frac{1}{2} \partial_t (\psi^*(x, t) \partial_x \psi(x, t) - \psi(x, t) \partial_x \psi^*(x, t)) , \quad (37)$$

which serves as the source term in the field equations. Since the macroscopic model involves averaging over microscopic volumes, it is sufficient to compute

only the expectation value. This can be conveniently obtained using the Ehrenfest theorem

$$\langle \partial_t j_Q \rangle (t) = \langle \psi(t) | \nabla V_C | \psi(t) \rangle + \mathcal{E}. \quad (38)$$

(see Appendix A for further context on the relation of the sources used for HHG and considered in Section 2 for CUPRAD).

Given $\psi(x, t)$, additional quantities can be calculated to provide deeper microscopic insight, such as the expectation value $\langle x \rangle$, the photoelectron spectrum [22], the volumetric and projected ground-state populations, and the energy distribution associated with ionisation [23]. Further analysis may include the Gabor transform of the source term, among others. Examples of specific analyses are discussed in Section 6, while the source term forms the basis for the transition to the macroscopic model of the XUV field.

3.2. XUV Propagation (Spectral Approach)

Compared to the infrared propagation (Section 2), we consider only linear effects for the propagation in the XUV region. It means that there is no feedback loop from the XUV field to HHG; and the XUV field can be retrieved by an integral transform of the macroscopic source terms $\widehat{\partial_t \mathbf{j}}_m$ in the whole interaction volume V_i .

Within the cylindrical symmetry, the far-field distribution in homogeneous generating media is given by [7]:

$$\widehat{\mathbf{E}}(\omega, \rho, z) \approx -\frac{\mu_0 e^{ik(\omega)z}}{4\pi} \times \int_{z_{\text{entry}}}^{z_{\text{exit}}} \frac{e^{-ik(\omega)z'} e^{i\frac{k(\omega)\rho^2}{2(z-z')}}}{z-z'} \int_{\Delta_T} e^{i\frac{k(\omega)(\rho')^2}{2(z-z')}} \left(\widehat{\frac{\partial \mathbf{j}_Q}{\partial t}} \right) J_0 \left(\frac{k(\omega)\rho\rho'}{z-z'} \right) \rho' d\rho' dz', \quad (39)$$

where (ρ', z') are the coordinates in the generating medium, and (ρ, z) specify the points in the far-field observation screen.³ The azimuthal angle is integrated out due to the cylindrical symmetry and the radial contributions are weighted by the Bessel function of the first kind J_0 . The interaction volume

³Note that $\widehat{\partial_t \mathbf{j}}_Q$ is the macroscopic dipole-acceleration density. The relation with the expected-value microscopic density is a simple scaling with the particle density ϱ in gas: $\widehat{\partial_t \mathbf{j}}_Q^{\text{macro}} = \varrho \left\langle \widehat{\partial_t \mathbf{j}}_Q^{\text{micro}} \right\rangle$.

$V_i = [z_{\text{entry}}, z_{\text{exit}}] \times \Delta_T$, where $[z_{\text{entry}}, z_{\text{exit}}]$ is the longitudinal dimension of the target and Δ_T is the transversal component. Note that the additional exponential factor in the Hankel transform, $\exp(\mathbf{i}k(\omega)(\rho')^2/2(z-z'))$, gives the solution of the paraxial wave equation incorporating the correction beyond the standard far-field diffraction. Namely, this propagator describes correctly Gaussian beams. This extended description was applied to successfully model the focusing properties of XUV beams [9].

We modify the expression (39) considering the density modulation. It changes the z' -dependent weight for each infinitesimal plane in the z' -integral. The signal from the plane is screened and dephased by the medium between the plane and the end of the medium. It effectively causes the replacement $k(\omega)z' \rightarrow \int_{z'}^{z_{\text{exit}}} k(\omega, z'') dz''$,

where $k(\omega, z)$ is the locally modulated dispersion relation including the absorption. Finally, considering the possible radial modulation, the far-field electric field is retrieved via

$$\hat{\mathbf{E}}(\omega, \rho, z) \approx -\frac{\mu_0 e^{\mathbf{i}k(\omega)z}}{4\pi} \int_{z_{\text{entry}}}^{z_{\text{exit}}} \int_{\Delta_T} \frac{e^{-\mathbf{i} \int_{z'}^{z_{\text{exit}}} k(z'', \rho', \omega) dz''} e^{\mathbf{i} \frac{k(\omega)\rho'^2}{2(z-z')}}}{z-z'} \times e^{\mathbf{i} \frac{k(\omega)(\rho')^2}{2(z-z')}} \left(\widehat{\frac{\partial \mathbf{j}_Q}{\partial t}} \right) J_0 \left(\frac{k(\omega)\rho\rho'}{z-z'} \right) \rho' d\rho' dz'. \quad (40)$$

More details about our particular implementation (such as the normalisation of the signal according to the absorption from a complex refractive index) are in the manual of the respective module.

We have finished the underlying theoretical description by the model of the XUV field. We thus can move to the practical numerical implementation of the respective modules.

4. A Modular Multiscale Approach (MMA): Implementations

The previous two sections established the physical model of all the involved processes. The next step is the numerical implementation. This section introduces the key algorithms and used methods and to facilitate the orientation in the codes, while details are left for the documentation [1].

4.1. A Parallel Radially Symmetric Unidirectional Solver (CUPRAD)

We briefly discuss some specifications related to the CUPRAD code. The simulation of pulsed-beam propagation in gases is very challenging from a

technical point of view and generally requires massively parallel computations. CUPRAD is written in Fortran90 and parallelized for distributed memory architecture by using the MPI (Message Passing Interface) library. Fast Fourier Transformations (FFT's) are performed by routines of the FFTW3 library.

A split-step scheme is employed for solving Equations (33) or (34) in radial symmetry. The basic idea of the split-step (or operator splitting) scheme is the following: We have an initial value problem

$$\frac{\partial}{\partial z}\psi = \hat{\mathcal{L}}\psi, \quad (41)$$

where $\hat{\mathcal{L}}$ is some operator. Our aim is an updating scheme to advance ψ from z to $z + \Delta z$, which we can formally write as

$$\psi(z + \Delta z) = e^{\int_z^{z+\Delta z} \hat{\mathcal{L}} dz} \psi(z), \quad (42)$$

where \int denotes $\int_z^{z+\Delta z}$. We suppose that $\hat{\mathcal{L}}$ can be written as a sum of m pieces

$$\hat{\mathcal{L}} = \hat{\mathcal{L}}_1 + \hat{\mathcal{L}}_2 + \dots + \hat{\mathcal{L}}_m, \quad (43)$$

and we know an updating scheme for ψ from z to $z + \Delta z$ for each piece, valid if that piece of the operator were the only one. Then, the straight forward split-step scheme is

$$\psi(z + \Delta z) = e^{\int_z^{z+\Delta z} \hat{\mathcal{L}}_1 dz} e^{\int_z^{z+\Delta z} \hat{\mathcal{L}}_2 dz} \dots e^{\int_z^{z+\Delta z} \hat{\mathcal{L}}_m dz} \psi(z), \quad (44)$$

and again \int denotes $\int_z^{z+\Delta z}$. Since in general the pieces $\int \hat{\mathcal{L}}_i dz$ do not commute, there is much to say about advancing the scheme by changing the order of the updating schemes $\exp(\int \hat{\mathcal{L}}_i dz)$ [24, 25]. However, in this short overview we restrict ourselves to the basic concepts and do not go into details.

A crucial thing in CUPRAD is to control the increment along the z axis, Δz , adaptively. In both Equation (33) and Equation (34) we split the operator $\hat{\mathcal{L}}$ into the linear part $\hat{\mathcal{L}}_{lin}$, containing diffraction and dispersion terms, respectively, and the nonlinear part $\hat{\mathcal{L}}_{nl}$ containing all other terms. We see that $\hat{\mathcal{L}}_{lin}$ is independent of z . Thus, here a constant step-size, determined by the transverse discretization, should be sufficient. In contrast, the nonlinear operator $\hat{\mathcal{L}}_{nl}$ is strongly dependent on z , and therefore decisive for adaptive step-size control. Let us show the principles by means of the simple example

$$\frac{\partial}{\partial z}\psi = \mathbf{i}\frac{\partial^2}{\partial t^2}\psi + \mathbf{i}|\psi|^2\psi. \quad (45)$$

Then we have $\hat{\mathcal{L}}_{lin} = \mathbf{i}\partial_t^2$ and $\hat{\mathcal{L}}_{nl} = \mathbf{i}|\psi|^2$. We have three constraints for Δz : The two advancing schemes $\exp(\int \hat{\mathcal{L}}_{lin} dz)$ and $\exp(\int \hat{\mathcal{L}}_{nl} dz)$ have to work, and Δz has to be small enough for our split-step scheme. The linear step can be achieved numerically exact in the Fourier space $\exp(\int \hat{\mathcal{L}}_{lin} dz) = \text{FFT}^{-1} \exp(-\mathbf{i}\omega^2 \Delta z) \text{FFT}$. Thus, there is no limitation for Δz from this scheme. For the nonlinear step we have to compute $\int |\psi|^2 dz \approx |\psi|^2 \Delta z$, the relative error of this approximation is $\sim |\psi|^4 \Delta z^2$. In order to control this relative error, we opt for $c_2 < |\psi|^2 \Delta z < c_1$. The constant c_1 guarantees a small enough error and $c_2 < c_1$ a preferably large step-size. The split-step scheme requires control of the size of $\|\hat{\mathbb{I}} - \exp(\int \hat{\mathcal{L}}_{lin} dz)\| \sim \Delta z / \Delta t^2$ and $\|\hat{\mathbb{I}} - \exp(\int \hat{\mathcal{L}}_{nl} dz)\| \sim |\psi|^2 \Delta z$, where Δt is the increment of the transverse coordinate t . Hence, we have to introduce a third constant $c_3 > \Delta z / \Delta t^2$. Because Δt is constant throughout the run, c_3 determines a second upper limit for Δz independent of $|\psi|^2$. It turned out that $c_1 = 0.01$, $c_2 = c_1 / 2.5$ and $c_3 = 1$ give reasonable results, provided that transverse discretization is sufficient.

CUPRAD solves Equations (33) and Equation (34) in radial symmetry, which means the transverse coordinates x and y are replaced by $r = \sqrt{x^2 + y^2}$. We split the operator of, e.g., Equation (34) into

$$\begin{aligned} \hat{\mathcal{L}}_{lin1} &= \frac{\mathbf{i}}{2k_0 r} \frac{\partial}{\partial r} \left(r \frac{\partial}{\partial r} \right), & \hat{\mathcal{L}}_{lin2} &= -\mathbf{i}k'' \frac{\partial^2}{\partial t^2}, \\ \hat{\mathcal{L}}_{nl} &= \mathbf{i}k_0 n_2 \int \mathcal{R}(t-t') |\mathcal{E}(t')|^2 dt' - \mathbf{i} \frac{k_0}{2\rho_c} \rho_e - U_i \frac{\mathcal{W}_{PI}}{2|\mathcal{E}|^2} \rho_{nt}, \end{aligned}$$

where we treat $\hat{\mathcal{L}}_{lin1}$ with a Crank-Nicholson scheme (see Ref. [24]), $\hat{\mathcal{L}}_{lin2}$ in Fourier space and $\hat{\mathcal{L}}_{nl}$ by multiplying with $\exp(\int \hat{\mathcal{L}}_{nl} dz)$. The integral is solved approximatively, in the easiest case we can take $\int_z^{z+\Delta z} \hat{\mathcal{L}}_{nl} dz \approx \hat{\mathcal{L}}_{nl}(z) \Delta z$. To perform the time integration for the delayed Kerr response and the electron density [Equation (15)] a simple Euler scheme (see Ref. [24]) works, provided that the time resolution is sufficiently fine. The boundaries of the numerical box are transparent ones in r [26]. Since the FFT's require periodic boundary conditions, a transparent box in t is not possible. However, a few (~ 16) absorbing layers give reasonable results, provided that the intensities of the fields that leave the box are small. The parallelization scheme relies on straightforward domain decomposition.

4.2. 1D-TSDE Implementation (CTDSE)

The computation of TDSE is implemented in the C language. It consists from the core CTDSE routine, which is used in two applications: The first application is the MPI-scheduler that processes the CUPRAD's output. This procedure is embarrassingly parallel, and the scheduler only assigns the macroscopic points with different inputs evenly to the CTDSE processes. The second application is the dynamically linked C-library, which is described in Section 6.

Here we outline the key methods implemented in the core routine. The wavefunction is directly represented on grids in both space and time. The grids are: $[-N_{x,\max}, \dots, 0, \dots, N_{x,\max}] \times \Delta x$ and $[0, \Delta t, \dots, N_{t,\max} \Delta t]$. The grid in time always starts at 0 for the purpose of CTDSE. The CTDSE module performs this transformation at the input from the interval $[t_{\min}, t_{\max}] \rightarrow [0, t_{\max} - t_{\min}]$. Since the discretisation in time for the CTDSE is usually finer than that of the CUPRAD, the input interface uses 0-padding in the Fourier space to interpolate the field for the required Δt .

Once the grids are set, we denote the wavefunction on the grids as $\psi(x_j, t_i) \equiv \psi_j^{(i)}$, in the vectorised form $\boldsymbol{\psi}^{(i)} \equiv (\psi_1^{(i)}, \psi_2^{(i)}, \dots, \psi_{2N_{x,\max}+1}^{(i)})^\top$. The advancement $\psi_j^{(i)} \rightarrow \psi_j^{(i+1)}$ is done in 3 substeps:

$$\boldsymbol{\psi}^{(i,1)} = \left(M_2 + \frac{\mathbf{i}\Delta t}{2} \left(-\frac{\Delta_2}{2} + M_2 V_C \right) \right) \boldsymbol{\psi}^{(i)}, \quad (46a)$$

$$\boldsymbol{\psi}^{(i,2)} = \left(M_2 - \frac{\mathbf{i}\Delta t}{2} \left(-\frac{\Delta_2}{2} + M_2 V_C \right) \right)^{-1} \boldsymbol{\psi}^{(i,1)}, \quad (46b)$$

$$\psi_j^{(i+1)} = \psi_j^{(i,3)} = e^{-\mathbf{i}\Delta t E(t_i) x_j} \psi_j^{(i,2)}, \quad \forall j. \quad (46c)$$

The first two substeps implement the Crank-Nicolson scheme for the field-free Hamiltonian using the improved Numerov's approximation of the Laplacian. The matrix representing the Numerov's refinement, M_2 , and the matrix representing the second-derivative, Δ_2 , are tridiagonal (see Section 3.1 of [27]) while the matrix potential, V_C , is local and, therefore, diagonal given by (36b) evaluated on the computational x -grid. All the operations thus involves only tridiagonal matrices and the inversion in (46b) can be done efficiently. The split-operator application of the field interaction is done in the third substep (46c). Note that the electric field varies usually much slower than the required t -discretisation. This means that this gives efficiently $\mathcal{O}(\Delta t^2)$ split-operator scheme.

All the desired outputs are computed directly on the x -grid. Most of them are implemented directly in the C-code for high performance. ψ itself is available as well for user-defined post-processing.

The actual implementation does not adopt any absorbing boundaries. One restriction is thus that the x -grid is required to be sufficiently large. In the present version of the code, there are no predictor corrector propropagation procedure. A fix time step of the output is needed to perform numerical Fourier transform. as detailed in the following, the TDSE will be run on different sets of electric field. To ensure converge, dt is fixed for converging the most complex field configuration of teh data set.

4.3. A Linear XUV Propagator (HANKEL)

Once the source terms $\widehat{\partial_{tj}j_Q}$ are computed in all the macroscopic points, they are inputted in the diffraction integral to get the macroscopic profile of the XUV field.

The computation of the Hankel transform is implemented in the Pythonic package `Hankel_transform`. We use a direct grid integration for evaluating (40). The model can access tabulated scattering factors. Therefore, the input is only the type of the gas and the source of the scattering tables. Regarding numerics, the (ρ, ω) -far-field plane is split into subarrays, which are then processed by OpenMPI (using the `multiprocessing` module). The module provides a wider interface to the routines. This provides versatility on the input side: the data can be fed directly or read from a drive on-the-fly. This could be important for memory-management of large datasets storing the dipole accelerations in the whole macroscopic volume. The details about the implementation and I/O are in the respective part of the documentation.

The module `Hankel_transform` can be used independently on the rest of the multiscale model. It provides the routine for long media that implements (40). Next, it also provides a lightweight routine for the usual Hankel transform from thin media.

5. Running The Model, User Interfaces

Here we introduce the execution pipeline of the model, show how to: provide a more advanced inputs to model more complex physical configurations; analyse and visualise the results. Finally, we detail the hdf5-structure used by the code.

5.1. Execution pipeline

Standard operation runs the modules on a supercomputer as a pipeline of consecutive jobs. The initial point is a starting hdf5-archive containing all the inputs. We provide two interfaces to create the starting file: a jupyter notebook and a transformer from a text-file input. The latter option is suitable for creating larger units to run the code many times to scan a subset of the parametric input space and similar tasks. Once the input file is ready, the pipeline is executed using a SLURM [28] queue of jobs.

There are basically two families of inputs: physical and numerical. The physical parameters describes the set up (the laser pulse at the entry of the simulation and the medium). Usually, the inputs are scalars, see below more advanced examples of customised inputs below. The second family of *physical* parameters are the *material constants*, which principally do not vary from one simulation to another. In our case, all these constants are related to the gas specie. There is a default option in the code for all the material constants, and the specification of the used gas is the only necessary input (note that all the material constants can be easily modified by a user within the input file if needed). Regarding the numerical parameters, the current release of the code require their specification because the code might be use for many different applications. The explanation of the input parameters is discussed in detail in the accompanying documentation. Next, we show test cases in Section 7.

5.2. Customised inputs

Here is a list of more complex input options, which allows for modelling more advanced physical configurations:

- *User-generated Ionization Rates:* CUPRAD includes, by default, a PPT-like ionization rates (see Appendix B.1.2 of [11] for the concrete implementation of the ionization model). The code can use an arbitrary ionization input by specifying the input `CUPRAD/inputs/ionization_model=ext`. Once applied, it requires a ionization-rate table (the values of the ionization rate as a function of the strength of the electric field) to be stored in the group `CUPRAD/ionisation_model`.
- *Inhomogeneous Gas Densities and Pre-Ionization:* An arbitrary density profile can be used in the model. It can be specified as a 2D map in the (ρ, z) -coordinates or as a 1D-array on the either of the coordinates. This allows us to model HHG in gas jets or even more complex

geometries [29, 30]. Similarly to the density profile, we can set a map of the pre-ionization: the initial electron density before the interaction.

- *User-generated Input Laser Pulses:* The versatility of the code is completed by implementing an arbitrary profile of the input laser pulse that are specified as functions $E(\rho, t)$. This feature is shown in Example 7.4.

5.3. Post-processing

Once the calculation is finished, the next step is to analyse and visualise the results. The code comes with a Pythonic loader of the CUPRAD data, which creates a class with data together with several methods to analyse them. The data from all the modules are then processed by Python. These methods and their uses are presented in Section 7 and in jupyter tutorials along the code [1].

5.4. HDF5 Data Structure

The main communication channel linking all the modules is the shared Hierarchical Data Format (specifically HDF5 [31]). All the data (both inputs and outputs) are then stored within the archive, let us call it `results.h5`. The philosophy is that every module reads inputs from its respective group in `results.h5` and stores all outputs therein. This structure is intended to be opaque for the standard operation introduced in the aforementioned sections. However, HDF5 provides both easy machine and human readability and it could be, therefore, easily customised to specific functionalities. To do so, the hdf5-archive structure is stored in 'h5namelists' (see the documentation [1] for details), reorganising the data structure then requires changing only these 3 lists; they shall be also used in all linked applications.

We use a descriptive approach in this section and focus on 1) the structure of the input for the whole model, 2) the final structure after all the modules finished the computation.

5.4.1. Input archive

The group for each of the modules contains the subgroup `inputs`, with all the input parameters (also including some pre-calculated tables as ionisation rates or the density-modulation profile). We discussed them in Section 5.2. Therein, we used a list of parameters in a free-form plain-text format or Pythonic approach to generate the inputs. In fact, all these approaches just wraps them into the hdf5-archive. Working directly with the hdf5-archives,

the presented input handling may be easily bypassed or modified to fit particular needs of users.

Let us look into more details on the inputs used to run CUPRAD that are stored within the CUPRAD group and global-inputs group. A test input is shown in Figure 1. It shows a typical input file for the simulation discussed in the example in Section 7.1. Some inputs are obligatory and a user has to provide them for every run. Some inputs are, however, optional with default hard-coded values. In all cases, all the inputs are filled in the input group by the pre-processor. For example, we use a simple specification of the gas by storing Ar in `global_inputs/gas_preset`. This invokes hard-coded values for the ionisation potential, dispersion tables, etc. tabulated in the code, these values are then added in the input group as well. The reason is that all the values are then always contained in the archive. We also employ the "hdf5-input-priority" policy, it means: if any of the input parameters is included in the input group, this value override the default hard-coded value.

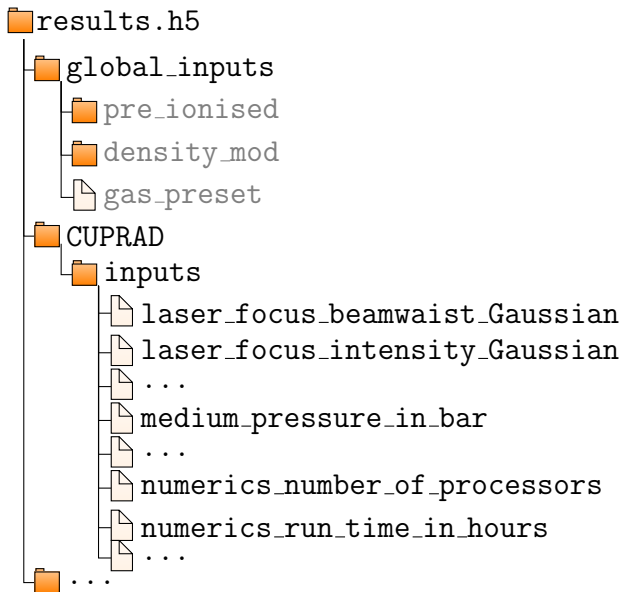


Figure 1: The HDF5-archove structure showing some of the CUPRAD inputs.

5.4.2. Output archive

The structure of the output archive is shown in Fig. 2.

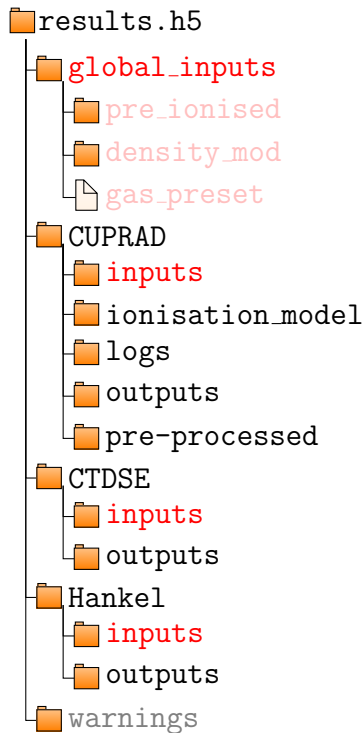


Figure 2: A schematic structure of the archive after all the modules finished the computation. Red groups shows the necessary inputs present before the execution of the respective module. Pink groups are optional inputs. Other groups contain the output data from the modules.

6. Interactive Python Interface to CTDSE (PyI-CTDE)

The TDSE code can be also individually accessed through a Pythonic interface relying on the Ctypes library, which provides access to low-level c-functions. The low-level computational routines are compiled from the same source as in the computational pipeline of the whole model, Subsection 5.1. An arbitrary input electric field can be used in PyI-CTDSE, which provides a user-friendly and flexible way to study the microscopic physics. Additionally to the solver itself, various analysing routines for the TDSE output, such as computation, of the photoelectron spectrum, Gabor transform, . . . , and the time-dependent wavefunction, are available as well.

An example of usage is in Section 7.5, more details about the implementation together with the full list of implemented C-analyses available directly from Python are directly in the documentation of the 1D-TDSE module [1].

One of more advanced analyses is the time-dependent electron energy density.

6.1. Analysing the Time-Dependent Electron Energy Density

One of the tools for providing a detailed microscopic insight is the photoelectron spectrum [22], which provides the energetic distribution of electrons after the interaction with the pulse. The structure includes, for example, above-threshold ionisation peaks, which are important to understand multiphoton processes. A special care is needed to extend this methodology to get insight into the process during the interaction because of the gauge freedom in the description of the interaction. We adopt the invariant methodology introduced in [23] (please find there the details about the treatment of the gauges). The resulting time-dependent energy distribution is

$$\mathcal{P}(E, t) = \lim_{\varepsilon \rightarrow 0} \langle \psi(t) | R_{H_0}(\varepsilon) | \psi(t) \rangle, \quad R_{H_0}(\varepsilon) = N_\varepsilon \varepsilon^2 ((E - H_0)^2 + \varepsilon^2)^{-1}, \quad (47)$$

where $|\psi(t)\rangle$ is expressed in the length gauge, $R_{H_0}(\varepsilon)$ is the resolvent operator corresponding to the field-free part of the Hamiltonian (36a) and N_ε is a normalisation factor the specific for a given numerical representation. It is convenient to compute⁴

$$\langle \psi(t) | \varepsilon^2 ((E - H_0)^2 + \varepsilon^2)^{-1} | \psi(t) \rangle = \| ((E - H_0) - \mathbf{i}\varepsilon)^{-1} \psi(t) \|^2, \quad (48)$$

where the inversion is done consistently with the numerical solver (46b).

7. Physics Examples & tutorials

Now, we present various features of the code suite by showing them in sample physical scenarios. We start with typical environments: a gas cell (Subsection 7.1) and gas jet with a Gaussian density profile (Subsection 7.2). Next, we move to more customised cases. We show the generation in a pre-ionised gas (Subsection 7.3), which is based on a previous physical application of the code suite [?]. We show how to implement user-provided input pulses (Subsection 7.4). Finally, we show the microscopic analysis of the time-dependent electron density (Subsection 6.1).

⁴Because H_0 is the only non-trivial operator in the expression, there is no commutativity issue and we can use $A^2 + B^2 = (A + \mathbf{i}B)(A - \mathbf{i}B)$.

Note that the main purpose of this section is to demonstrate the current capabilities of the code and typical accessible characteristics. Each of the following examples is treated in more details in a respective tutorial implemented in a jupyter notebook where more details are present.

7.1. HHG in a Gas-Cell

The default option to run the code is a Gaussian beam and pulse entering a gas cell with a homogeneous density. To present this basic mode of operation, we consider a Gaussian 30-fs laser pulse (defined by the intensity dropping to $1/e^2$ of the peak focus intensity) with the waist $w_0 = 100 \mu\text{m}$. The peak intensity is set to approximately $2.44 \times 10^{14} \text{ W/cm}^2$, which corresponds to the extent of the harmonic plateau up to the 40th harmonic according to the classical cut-off law, $E_{\text{cut-off}} = I_p + 3.17U_p$ [32]. Because $E_{\text{cut-off}}$ is linearly proportional to the intensity through U_p , it provides a convenient way to measure the intensity, which we adapt in our examples. Then we place a 1-cm-long gas cell filled by argon at 25 mbar in the path of the beam keeping the original focus in the middle of the cell.

Figure 3 shows the 1) distortion of the pulse due to the non-linear propagation and, 2) the corresponding degrees of ionisation. The pulse at the exit of the cell, Fig. 3b), exhibits the reduction of the peak intensity due to defocusing and the redistribution of the intensity into the off-axis "wings" of the pulse. This behaviour is explained by the plasma defocusing: The free electrons, Fig. 3c), reduces the refractive index in the region with the free electrons. This effectively forms a diverging lens for the subsequent portion of the pulse.

The next steps of the pipeline compute all the dipoles induced in the macroscopic volume and then integrates the produced XUV signal via the means of the Hankel transform. The harmonic spectra are shown in Fig. 4. The code can store—for a reference—the transforms of the entry and exit planes. As the entry pulse is Gaussian both in space and time, the entry-plane transform in Fig. 4a) contains typical ring structures (cf. Fig. 8 of [7]). The result of the interest for applications is the integrated harmonic spectrum shown in different scales in Figs. 4c,d).

In summary, this shows the simple mode of operation showing the visualisations of the usual quantities of interest.

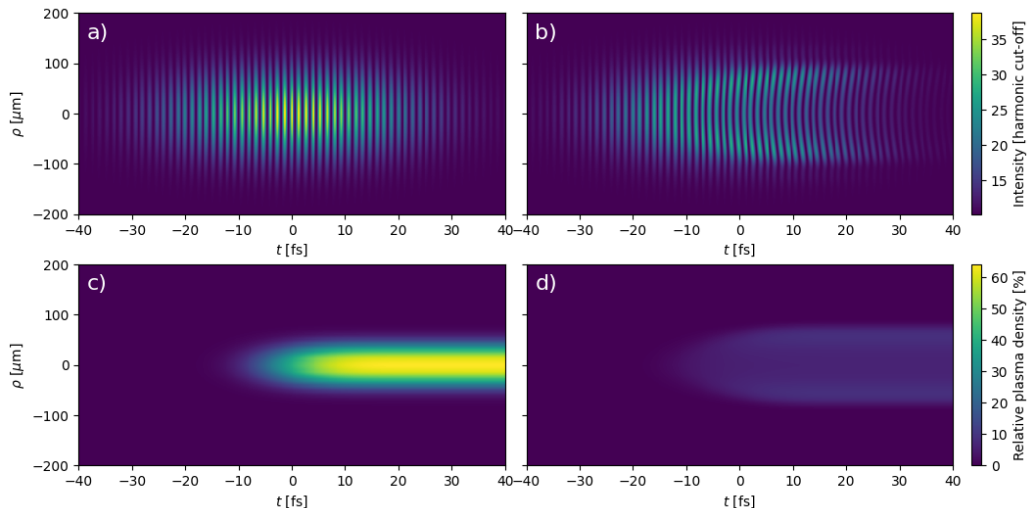


Figure 3: The initially Gaussian pulse in time t and radial coordinate ρ expressed in the units of harmonic cut-off in panel a) propagates through 1-cm-long 25-mbar argon gas cell leading to a distorted pulse b). The bottom panels c,d) shows the respective plasma profiles.

7.2. HHG in a Gas-Jet

This example extends the capabilities of the code to simulate the propagation in a density-modulated medium. A simple example is a gas jet. We focus a 15-fs, 100- μm Gaussian pulse (referred by the parameters in the focus) in the middle of a Gaussian pressure profile $p(z) = p_0 \exp(-(z/a)^2)$ with $a = 5/4$ mm and $p_0 = 50$ mbar.

Figure 5a) shows the density profile and cumulative signals for harmonics indicated in the spatially-resolved far-field spectrum shown in Fig. 5b).

7.3. Absorption-limited HHG with Pre-Ionization in a Gas-Cell

This example is based on the application of the full code in designing an optimisation scheme for HHG by homogeneously pre-ionising the medium [10], the free electrons increase the driver's phase velocity enabling to catch-up the harmonic field and efficiently phase-match the generation process. Instead of the physical context that is treated in detail in the reference, we present the further capabilities of the code.

We focus a 45-fs, 100- μm Gaussian pulse (referred by the parameters in the focus) in the middle of 15-mm-long gas cell filled by krypton at 25 mbar.

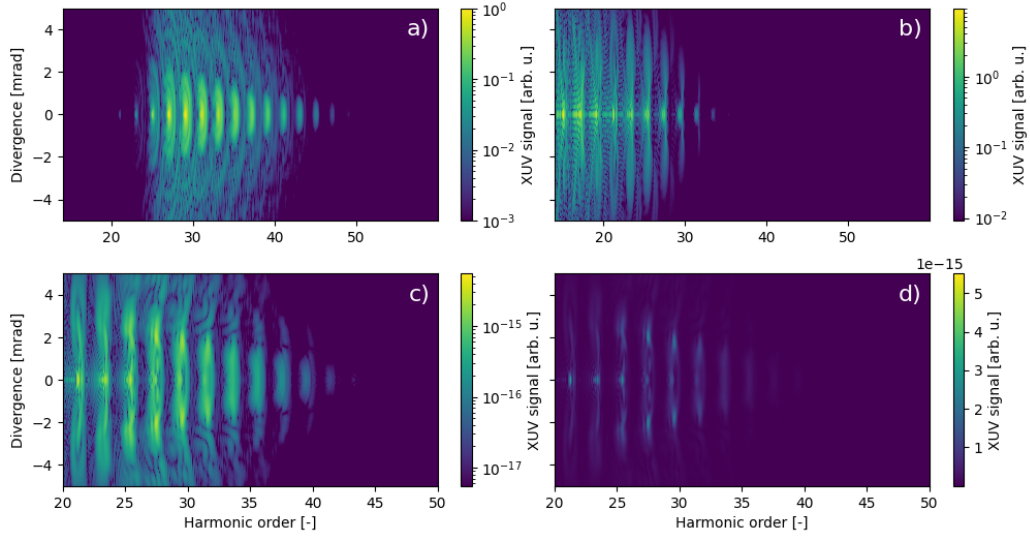


Figure 4: Spatially resolved far-field harmonic spectra: a) and b) the transforms of the sources in the entry and exit plane respectively, corresponding to the pulse-propagation shown in Fig. 3; c) and d) the harmonic signal integrated along the whole interacting volume in different scales.

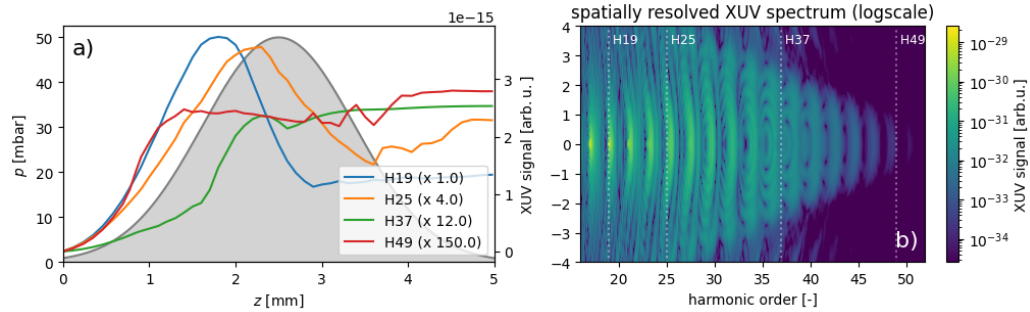


Figure 5: The propagation in a gas jet described in Section Physical examples: HHG in a Gas-Jet. a): The pressure profile and the build up of the harmonic signals for the selected harmonics. b) Spatially resolved far-field harmonic spectrum.

The medium is initially pre-ionised to 0.9 times the optimal pre-ionisation value defined by the equality of the phase velocities for IR and the 17th harmonic [10].

The following analyses shows how to get more advanced analyses using

the complexified representation of the pulse envelope defined as

$$\mathcal{E}_{ce}(t) = e^{i\omega_0 t} \mathcal{E}_c(t), \quad \mathcal{E}_c(t) = \mathcal{F}^{(-1)} [\theta_H(\omega) \mathcal{F} [E(t)] (\omega)] (t), \quad (49)$$

where θ_H is the Heaviside function and \mathcal{F} denotes the Fourier transform (we omitted the unaffected spatial coordinates). This representation provides elegant access to various pulse characteristics. First, the original field is the real part of the complexification $E(t, \mathbf{r}) = \text{Re } \mathcal{E}_c(t, \mathbf{r})$. Next, the envelope of the pulse is $|\mathcal{E}_c(t, \mathbf{r})| = |\mathcal{E}_{ce}(t, \mathbf{r})|$. Finally, the spatiotemporal phase deviation of the field with respect to the monochromatic carrying wave is retrieved as $\Phi(t, \mathbf{r}) = \text{Arg}(\mathcal{E}_{ce}(t, \mathbf{r}))$.

Figure 6a) shows the spatial intensity profile corresponding to $\max_t |\mathcal{E}_{ce}(t, \mathbf{r})|^2$. It shows the intensity clamping inside the first third of the medium and then a stable slow decrease in the rest of the medium, which is the region of the interest contributing to the harmonic signal [10]. Figure 6b) shows that the homogeneous pre-ionisation does not affect the propagation and that the additional pre-ionisation add almost constant addition plasma density in the region of the interest.

Figures 6c,d) shows coherence maps for the 17th harmonic. This metric [33] allows for estimating the size of a macroscopic volume where all the microscopic emitters add up constructively. It is inferred from three different contributions: 1) local dephasing of the driver's field $\partial_z \Phi$; 2) the dispersive properties of the harmonic field $\Delta k_{XUV} = (\omega_{17}/c)(n(\omega_{17}) - 1)$ obtained from the refractive index $n(\omega)$; and 3) the dephasing of the microscopic dipoles, which can be fairly modelled as linearly proportional to the longitudinal gradient of the driver's intensity $\Delta k_{\text{dipole}} \approx -\alpha_{\text{H17}}(I_{\text{IR}})\partial_z I_{\text{IR}}$. In summary

$$L_{\text{coh, H17}} = \frac{\pi}{|\partial_z \Phi + \Delta k_{\text{XUV}} - \alpha_{\text{H17}}(I_{\text{IR}})\partial_z I_{\text{IR}}|}. \quad (50)$$

(See the Supplement of [10] for a detailed derivation.) The quantities entering (50) are then retrieved: Φ and $I_{\text{IR}} \sim |\mathcal{E}_{ce}|^2$ directly from the CUPRAD outputs; Δk_{XUV} from dispersion tables [34, 35]; and α_{H17} by solving a set of non-linear equations under the Strong-Field Approximations, presented for example in [36]. Therefore, L_{coh} provides us insight in the high-harmonic generation without computing TDSE. In this case, it shows that the optimal phase-matching conditions are reached in the pre-ionised target, Fig. 6d).

In conclusion, we have presented one of real applications of the code together with closer analyses derived from the numerical solution of the CUPRAD component.

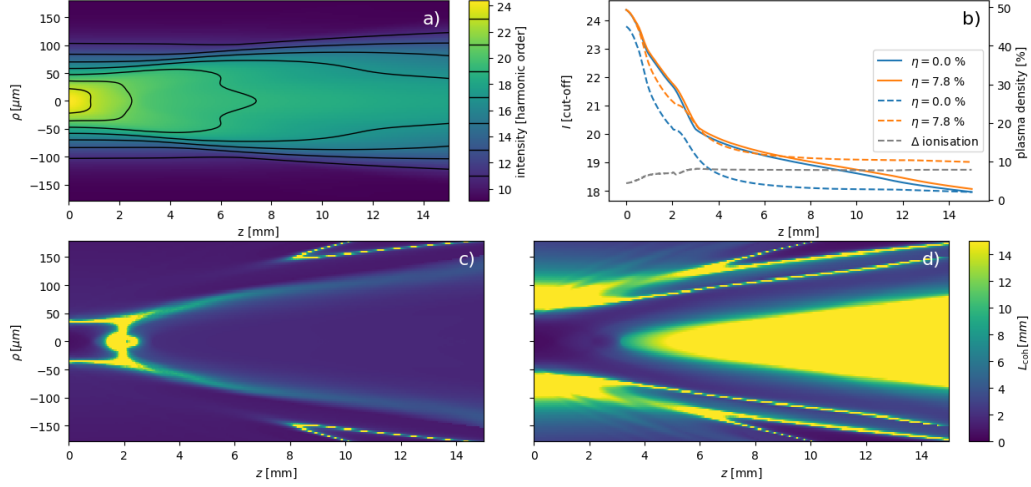


Figure 6: a): The spatial maxima of the intensity profile $\max_t I_{\text{IR}}(z, \rho, t)$ according to the parameters described in Section 7.3. b): The on-axis ($\rho = 0$) intensity profiles with and without the pre-ionisation given by η (full-lines). The η -value maximise (50) for an idealised plane-wave propagation. The ionisation degrees for these cases after the passage of the pulse (corresponding dashed lines) and Δ ionisation as the difference between these two values. The bottom panels c,d) show the coherence maps (50) evaluated at times corresponding to the intensity maxima.

7.4. HHG with Bessel-Gauss Beams

This example shows how to use a custom input field. The current release of the code requires to add this field in the appropriate hdf5 group created by the CUPRAD pre-processor. This group contains complexified electric field (49) in the entry plane. We replace it by a Bessel-Gauss profile. We will not compute HHG in this section to just show the usage of CUPRAD as an independent module.

The input electric field profile for the Bessel-Gauss pulse is [37]:

$$E(\rho, t) = E_0 e^{-\left(\frac{\rho}{w_0}\right)^2 - \left(\frac{t}{\tau}\right)^2} J_0\left(\frac{2r\rho}{w_0}\right) \cos(\omega_0 t), \quad (51)$$

where J_0 is the Bessel function of the first kind. The parameter r defines the portion of the Bessel contribution to the pulse (we have usual Gaussian beam for $r = 0$).

We consider a 30-fs Bessel-Gauss pulse with peak intensity $I_0 \approx 1.7 \times 10^{14}$ W/cm² focused at the entry of 8-cm long gas cell filled by argon at

25 mbar. We set the Bessel contribution $r = 5$ and find appropriate value of w_0 such that the waist of the full Bessel-Gauss beam (defined by the $1/e^2$ -drop in the intensity) is $50 \mu\text{m}$. Figure 7 studies the propagation of this pulse. The input pulse is shown in Fig. 7a). While the pulse after the propagation still preserved the central part, there is clearly present a planar diverging off-axis part of the pulse. Figures 7c,d) provides a comparison with a purely Gaussian beam ($r = 0$) with the exactly same entry beam-radius. It shows that the focus of the Bessel-Gauss beam is much longer.

In conclusion, we have demonstrated the capability of the code to simulate arbitrary input pulse profile.

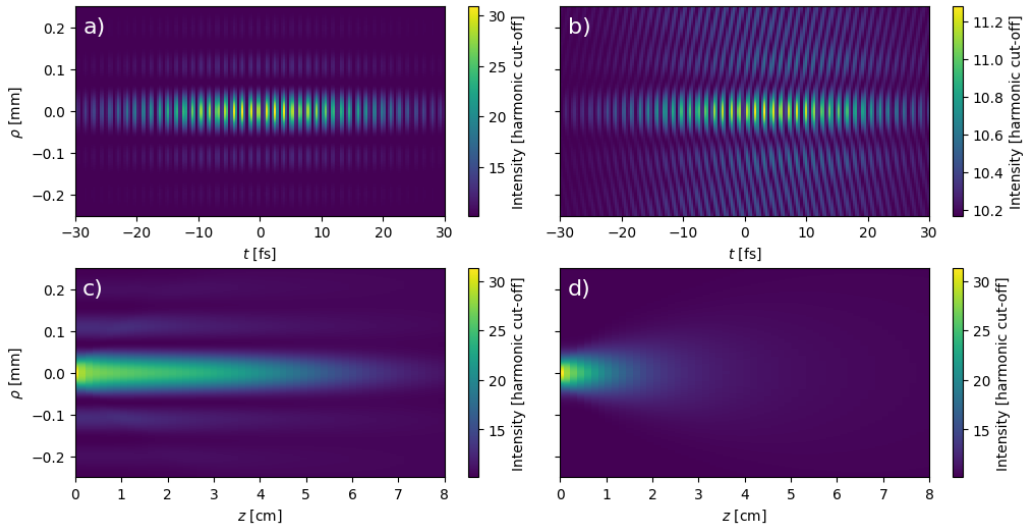


Figure 7: The characterisation of the Bessel-Gauss pulse propagation. a): The initial intensity profile corresponding to the Bessel-Gauss pulse at focus with the parameters described in Section 7.4. b): The pulse after the propagation through the 8-cm argon cell. c): The peak-intensity profile along the propagation, d): The purely Gaussian pulse with the same waist as for the Bessel-Gauss pulse.

7.5. Microscopic insights

Finally, we address the microscopic solver, which is both part of the computational pipeline of the whole macroscopic model and accessible directly from Python described in Section 6. We show an example of analysing the 1D-TDSE outputs below.

We show an example of a chirped pulse, Fig. 8a), interacting with an argon atom defined by the soft-Coulomb potential (36b). Figure 8b) shows the dipole acceleration (37), which is the source term of the XUV field. A further insight in the interaction is retrieved by analysing the wavefunction, Fig. 8c). One example is the Gabor transform, Fig. 8d), which provides frequency-temporal resolution of the process. Simply said, it tells us when a given frequency (therefore the corresponding XUV photon energy) is generated within the pulse. In the case of the HHG process the arcs reveal the contribution of short trajectories in the rising part reaching the cut-off region at their tops then falling along the recombinations of long trajectories [38]. Figure 8e) present a more advanced analysis of invariant photoelectron’s energetic distribution (see [23] for the methodology) and derived population of the ground state compared with the volumetric probability of finding electron in the vicinity of the nucleus, Fig. 8f).

In summary, the Pythonic interface to the TDSE solver together with related analyses provide a powerful flexible tool for getting insight in the microscopic dynamics.

8. Conclusions and perspectives

We have presented a code suite with the primary objective to model HHG in noble gases. In summary, the first release consists of three main modules:

1. CUPRAD: The code for solving the IR pulse propagation in a macroscopic interaction volume. It supports the propagation of linearly polarised pulses in cylindrical symmetry. The code is implemented in Fortran and employs MPI parallelisation.
2. CTDSE: The 1D-TDSE code for solving the microscopic response in all the points in the macroscopic medium. The code is implemented in c, and it comes with a Pythonic interface. In the context of the multiscale model, the task is principally embarrassingly parallel using MPI.
3. XUV diffraction: It includes diffraction integral to collect all the microscopic emitters, the code is implemented in Python using multiprocessing parallelisation.

The code is accompanied by Pythonic pre- and post-processing, which provides a way to easily define input physical setup and visualise output data. The communication relies on HDF5-data format, which provides both interfaces between different modules and a convenient way to access data in a human-readable format.

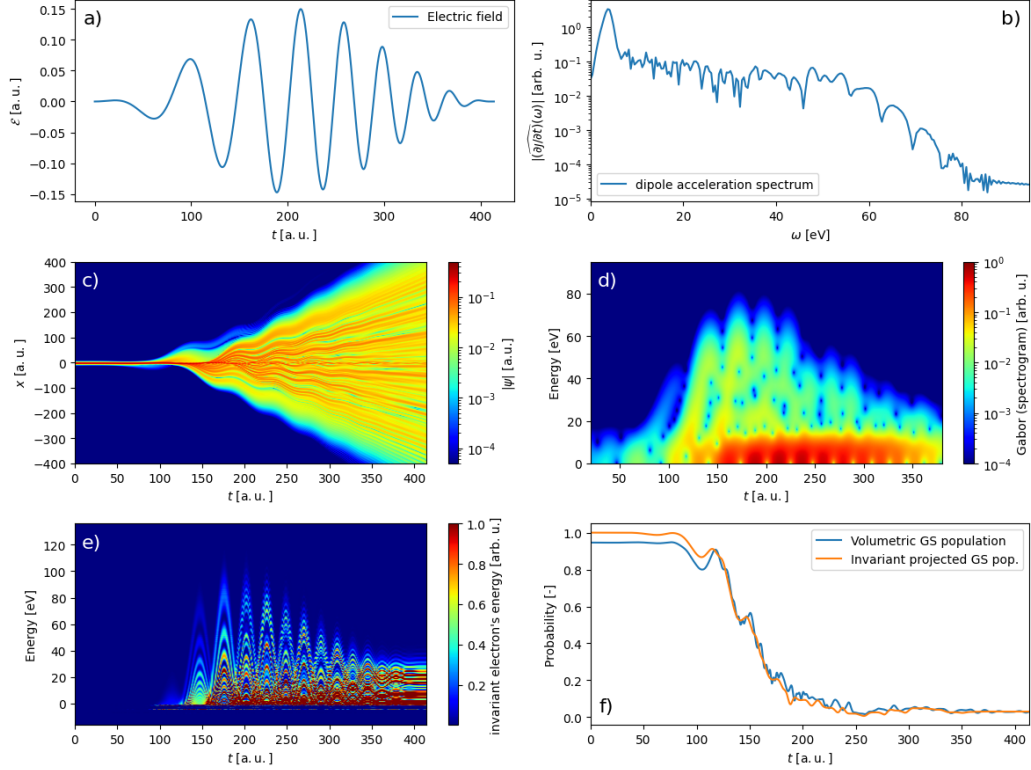


Figure 8: The analysis of the 1D-argon atom interaction with the chirped pulse defined in panel a). The dipole-acceleration (37) spectrum is shown in panel b). Panel c) shows the wavefunction modulus $|\psi(x, t)|$, note the various portions of the wavepacked driven by the oscillating field. Panel d) shows the Gabor transform of $\partial_t j_Q$. Panel e) shows the time-resolved energetic distribution of the photoelectron and panel f) the corresponding populations of the ground state.

Despite the limiting assumptions in the first release, the code has already proven its applicability for various HHG-related problems to obtain results in collaboration with experimentalists. The code is under active development with some of the future modules already in preparation. The actual roadmap follows: The next release shall include 3D-pulse propagation with arbitrary polarisation, propagation in capillaries, optimised 1D-TDSE employing 1D-potentials and more numerical and modelling features, 3D-TDSE for arbitrarily polarised pulses, SFA-like microscopic responses, and near-field XUV propagator. Together with the new modules, the documentation and tutorials shall be improved. All these modules are already of practical

use of the developer’s institutes, which means direct motivations for prioritising the features in development. The huge palette of tools is desired as it might provide an optimal trade-off between the physical effects captured in the simulations and the computational cost per simulation.

One objective of the development is to ensure straightforward usability of the open-source package.

- *User side:* The code is accompanied by Jupyter-notebook tutorials, a Docker container for local execution, and installation notes for HPC clusters. The latter have been tested on several architectures with both Slurm and PBS schedulers. All documentation is bundled with the first public release in the Git repository [1].
- *Developer side:* A defined software architecture—clear module interfaces and reproducible computational pipelines—provides a substrate on which computational physicists in HHG and related fields can contribute additional modules.

In summary, the project initiates a community effort that links theoretical and numerical specialists in HHG with experimental and engineering users who may employ the code to design XUV beamlines (e.g. [39]) and to plan dedicated experiments.

Appendix A. Microscopic source terms

The goal of this appendix is to provide further physical context on the assumptions used for modelling the non-linear source term for CUPRAD and computed from TDSE via (37). The main difference comes already from the initial assumptions in the derivation of CUPRAD, starting from the macroscopic version of Maxwell’s equation (1), which already contains the microscopically averaged source terms [40] assumed in (1a) and (1d).

The main difference is in the different spectral and intensity ranges of interest for the two parts. We start with the IR-propagation that stays spectrally below the ionisation threshold and the main contributions arises from the atomic structure of bound electrons expressed in the expansion of the non-linear polarisation $\mathbf{P}^{(i)}$ (6) and (14), free electrons due to the ionisation and finally, and the ionisation and recombination process itself (these two processes are contained together in (20)). These effects relies on the full structure of atom and it would require 3D-TDSE or even beyond to

cover multi-electronic structure of the bound electrons. Fortunately, this is fairly modelled by the means of standard linear and non-linear optics, which provide reliable and widely tested tools for the modelling.

The situation is different for HHG, this process comes from the dynamics of the single active electron involved in the "three-step-process" [32]. It turns out that the main aspects of this process are fairly included already in the limited 1D-geometry. Particularly, the exact sub-cycle structure of the driving electric field becomes important, which is already precisely included in the 1D-TDSE.

Let us now link more closely the currents averaged by (38) and the macroscopic version in the Maxwell's equations (1). We write respectively the expected value of the current density and its derivative using the Ehrenfest theorem. Next, we use the potentials ϕ and \mathbf{A} (manifesting the gauge-invariance) to describe the external field and keeping full-dimensionality. These quantities read

$$\langle \mathbf{j}(t) \rangle = - \langle \psi(t) | \mathbf{p} + \mathbf{A}(t) | \psi(t) \rangle , \quad (\text{A.1a})$$

$$\begin{aligned} \langle \partial_t \mathbf{j}(t) \rangle &= \langle \psi(t) | \nabla (V_c - \phi(t)) - \partial_t \mathbf{A}(t) | \psi(t) \rangle = \\ &\langle \psi(t) | \nabla V_c + \mathcal{E}(t) | \psi(t) \rangle . \end{aligned} \quad (\text{A.1b})$$

Note that all expression are expressed in 3D but are computed so far in 1D in the present version of the code; and the last expression manifestly contains \mathcal{E} regardless the choice of the gauge. In our 1D version of the code, the length gauge is used and expected value is written down as

$$\partial_t \mathbf{j}(t) = \int dx \psi^*(x, t) \psi(x, t) (\partial_x V_c(x) + \mathcal{E}(t)) . \quad (\text{A.2})$$

What is the link between \mathbf{P} and \mathbf{J} defined in the Eq. (1d) for solving the Maxwell equations and the one obtained from the TDSE? There are two aspect to consider: i- the meaning the quantity ii- and how to relate them to go from the microscopic world to the macroscopic quantities as used in the Maxwell solver. Concerning the meaning the meaning of the microscopic \mathbf{P} and macroscopic counterpart are indeed different. In the microscopic case, it concerns the total polarisation of the considered system. While in the case of macroscopic term, it refers explicitly to bound-bound transition. The same occurs of the current of charge. In the microscopic world it is the total current (so that $\mathbf{J}(t) = \partial_t \mathbf{P}(t)$) while in the maxwell's equations it refers to the free electrons dynamics. Bound-bound or Continuum-Continuum transition of

course can be extracted following the work presented in [22], thus allowing for instance the retrieval of the Brunel formula obtained in the classical limit REF. Ionization dynamics can be extracted also that way and is described in more detail in Sec. 6.1. What is used in the present version of the code is Eq. A.1b. The link between the microscopic current and macroscopic equivalent (total current) assumes that the medium is tenuous so that all atoms can be treated independantly. The total macroscopic current is then:

$$\partial_t \mathbf{J}_m(t) = \rho_0(r, t) \partial_t \mathbf{j}(t), \quad (\text{A.3})$$

where $\rho_0(r, t)$ is the time and space dependent gas density. In the present version of the code, the gas density is time-independent, the spatial dependence is implemented, see Section 7.2.

Appendix B. Acknowledgements and author contributions:

J.V. is the main designer of interfaces between the modules, the architect of the data-structure. He participated in the development of all the modules and adapted them for specific tasks. He is the main author of the Hankel module. He designed i) a part of the main CTDSE routines and its parallelisation, ii) computational pipelines and tutorials. *T.N.* refactored the c-code for the CTDSE solver and developed the Pythonic interface of CTDSE; he worked on the deployment of the code and installation tools. *S.S.* is the main author of CUPRAD, including core routines, parallelisation, and physical model. *F.C.* is the main author of CTDSE and the physical model of the Hankel module. All the authors contributed to the writing of the manuscript, documentation, and reviewed the work on the whole project. *J.V.* acknowledges the support by the project Advanced Research Using High Intensity Laser Produced Photons and Particles (CZ.02.1.01/0.0/0.0/16_019/0000789) from the European Regional Development Fund (ADONIS). We acknowledge various providers of the computer time during the development: 1) the SUNRISE cluster at ELI-Beamlines facility and *J.V.* acknowledges great support from Edwin Chacón-Golcher. 2) This work was supported by the Ministry of Education, Youth and Sports of the Czech Republic through the e-INFRA CZ (ID:90254). 3) Computer time for this study was provided by the computing facilities of the MCIA (Mésocentre de Calcul Intensif Aquitain). 4) the Grand

Equipement National de Calcul Intensif (GENCI project A0120507594). Finally we acknowledge the feedback from all our collaborators on the applications of the code [9] and [10].

References

- [1] J. Vábek, T. Němec, S. Skupin, F. Catoire, Multiscale modular approach (MMA) for HHG modelling (Jul. 2025).
URL <https://github.com/HHG-modelling/MMA-HHG-pre-release-2>
- [2] M. Lewenstein, P. Balcou, M. Y. Ivanov, A. L’Huillier, P. B. Corkum, Theory of high-harmonic generation by low-frequency laser fields, *Phys. Rev. A* 49 (1994) 2117–2132. doi:10.1103/PhysRevA.49.2117.
URL <https://link.aps.org/doi/10.1103/PhysRevA.49.2117>
- [3] F. Calegari, G. Sansone, S. Stagira, C. Vozzi, M. Nisoli, Advances in attosecond science, *Journal of Physics B: Atomic, Molecular and Optical Physics* 49 (6) (2016) 062001. doi:10.1088/0953-4075/49/6/062001.
URL <https://dx.doi.org/10.1088/0953-4075/49/6/062001>
- [4] R. Weissenbilder, S. Carlström, L. Rego, C. Guo, C. M. Heyl, P. Smorenburg, E. Constant, C. L. Arnold, A. L’Huillier, How to optimize high-order harmonic generation in gases, *Nature Reviews Physics* 4 (11) (2022) 713–722. doi:10.1038/s42254-022-00522-7.
URL <http://dx.doi.org/10.1038/s42254-022-00522-7>
- [5] D. Castelvetti, K. Sanderson, Physicists who built ultrafast ‘attosecond’ lasers win nobel prize, *Nature* 622 (7982) (2023) 225–227.
- [6] E. Constant, S. Nandi, C. Picot, E. Prost, S. Palakkal, F. Lépine, V. Loriot, High order harmonic generation-based attosecond light sources and applications to quantum phenomena, *APL Photonics* 10 (1) (Jan. 2025). doi:10.1063/5.0235171.
URL <http://dx.doi.org/10.1063/5.0235171>
- [7] F. Catoire, A. Ferré, O. Hort, A. Dubrouil, L. Quintard, D. Descamps, S. Petit, F. Burgy, E. Mével, Y. Mairesse, E. Constant, Complex structure of spatially resolved high-order-harmonic spectra, *Phys. Rev. A* 94 (2016) 063401. doi:10.1103/PhysRevA.94.063401.
URL <https://link.aps.org/doi/10.1103/PhysRevA.94.063401>

- [8] L. Quintard, V. Strelkov, J. Vabek, O. Hort, A. Dubrouil, D. Descamps, F. Burgy, C. Péjot, E. Mével, F. Catoire, E. Constant, Optics-less focusing of xuv high-order harmonics, *Science Advances* 5 (4) (2019) eaau7175. arXiv:<https://www.science.org/doi/pdf/10.1126/sciadv.aau7175>, doi:10.1126/sciadv.aau7175. URL <https://www.science.org/doi/abs/10.1126/sciadv.aau7175>
- [9] K. Veyrinas, J. Vábek, C. Valentin, D. Descamps, C. Péjot, F. Burgy, E. Constant, E. Mével, F. Catoire, Spectral filtering of high-order harmonics via optics-free focusing, *Opt. Express* 29 (19) (2021) 29813–29827. doi:10.1364/OE.436086. URL <https://opg.optica.org/oe/abstract.cfm?URI=oe-29-19-29813>
- [10] O. Finke, J. Vábek, M. Nevrkla, N. Bobrova, O. Hort, L. Jurkovičová, M. Albrecht, A. Jančárek, F. Catoire, S. Skupin, J. Nejdil, Phase-matched high-order harmonic generation in pre-ionized noble gases, *Scientific Reports* 12 (1) (May 2022). doi:10.1038/s41598-022-11313-6. URL <http://dx.doi.org/10.1038/s41598-022-11313-6>
- [11] L. Bergé, S. Skupin, R. Nuter, J. Kasparian, J.-P. Wolf, Ultrashort filaments of light in weakly ionized, optically transparent media, *Reports on Progress in Physics* 70 (10) (2007) 1633. doi:10.1088/0034-4885/70/10/R03. URL <https://dx.doi.org/10.1088/0034-4885/70/10/R03>
- [12] A. Couairon, A. Mysyrowicz, Femtosecond filamentation in transparent media, *Physics Reports* 441 (2) (2007) 47–189. doi:<https://doi.org/10.1016/j.physrep.2006.12.005>. URL <https://www.sciencedirect.com/science/article/pii/S037015730700021X>
- [13] T. Brabec, F. Krausz, Nonlinear optical pulse propagation in the single-cycle regime, *Phys. Rev. Lett.* 78 (1997) 3282.
- [14] M. Kolesik, J. V. Moloney, Nonlinear optical pulse propagation simulation: From Maxwell's to unidirectional equations, *Phys. Rev. E* 70 (3) (2004) 036604.
- [15] R. Boyd, *Nonlinear Optics*, third edition Edition, Academic Press, Burlington, 2008.

- [16] A. M. Perelomov, V. S. Popov, M. V. Terent'ev, Ionization of atoms in an alternating electric field, *JETP Lett.* 23 (1966) 924.
- [17] K. Sallai, S. Hack, S. Majorosi, A. Czirják, One-dimensional model potentials optimized for the calculation of high-order-harmonic-generation spectra, *Phys. Rev. A* 110 (2024) 063117. doi:10.1103/PhysRevA.110.063117.
URL <https://link.aps.org/doi/10.1103/PhysRevA.110.063117>
- [18] F. He, C. Ruiz, A. Becker, Absorbing boundaries in numerical solutions of the time-dependent schrödinger equation on a grid using exterior complex scaling, *Phys. Rev. A* 75 (2007) 053407. doi:10.1103/PhysRevA.75.053407.
URL <https://link.aps.org/doi/10.1103/PhysRevA.75.053407>
- [19] Y. Orimo, T. Sato, A. Scrinzi, K. L. Ishikawa, Implementation of the infinite-range exterior complex scaling to the time-dependent complete-active-space self-consistent-field method, *Phys. Rev. A* 97 (2018) 023423. doi:10.1103/PhysRevA.97.023423.
URL <https://link.aps.org/doi/10.1103/PhysRevA.97.023423>
- [20] D. Jelovina, J. Feist, F. Martín, A. Palacios, Finite element dvr method for molecular single and double ionization by strong laser pulses, *Journal of Physics: Conference Series* 635 (11) (2015) 112042. doi:10.1088/1742-6596/635/11/112042.
URL <https://dx.doi.org/10.1088/1742-6596/635/11/112042>
- [21] J. D. Jackson, *Classical electrodynamics*, 3rd Edition, Wiley, New York, NY, 1999.
URL <http://cdsweb.cern.ch/record/490457>
- [22] F. Catoire, H. Bachau, Extraction of the absolute value of the photoelectron spectrum probability density by means of the resolvent technique, *Phys. Rev. A* 85 (2012) 023422. doi:10.1103/PhysRevA.85.023422.
URL <https://link.aps.org/doi/10.1103/PhysRevA.85.023422>
- [23] J. Vábek, H. Bachau, F. Catoire, Ionization dynamics and gauge invariance, *Phys. Rev. A* 106 (2022) 053115. doi:10.1103/PhysRevA.106.053115.
URL <https://link.aps.org/doi/10.1103/PhysRevA.106.053115>

- [24] W. H. Press, B. P. Flannery, S. A. Teukolsky, W. T. Vetterling, Numerical Recipes, Cambridge University Press, Cambridge, 1989.
- [25] A. C. Newell, J. V. Moloney, Nonlinear Optics, Addison-Wesley, Reading, MA, 1992.
- [26] G. R. Hadley, Transparent boundary condition for beam propagation, *Opt. Lett.* 16 (9) (1991) 624–626. doi:10.1364/OL.16.000624.
URL <https://opg.optica.org/ol/abstract.cfm?URI=ol-16-9-624>
- [27] H. G. Muller, An efficient propagation scheme for the time-dependent schroedinger equation in the velocity gauge, *Laser Physics* 9 (1999) 138–148.
- [28] M. A. Jette, T. Wickberg, Architecture of the slurm workload manager, in: D. Klusáček, J. Corbalán, G. P. Rodrigo (Eds.), *Job Scheduling Strategies for Parallel Processing*, Springer Nature Switzerland, Cham, 2023, pp. 3–23.
- [29] V. V. Strelkov, R. A. Ganeev, Quasi-phase-matching of high-order harmonics in plasma plumes: theory and experiment, *Opt. Express* 25 (18) (2017) 21068–21083. doi:10.1364/OE.25.021068.
URL <https://opg.optica.org/oe/abstract.cfm?URI=oe-25-18-21068>
- [30] O. Finke, J. Vábek, M. Dvořáček, L. Jurkovičová, M. Albrecht, H. Ovcharenko, O. Hort, J. Nejd, Monochromatic high-order harmonic generation by a besel-gauss beam in periodically modulated media, *Phys. Rev. A* 109 (2024) 033517. doi:10.1103/PhysRevA.109.033517.
URL <https://link.aps.org/doi/10.1103/PhysRevA.109.033517>
- [31] The HDF Group, Hierarchical Data Format, version 5.
URL <https://github.com/HDFGroup/hdf5>
- [32] P. B. Corkum, Plasma perspective on strong field multi-photon ionization, *Phys. Rev. Lett.* 71 (1993) 1994–1997. doi:10.1103/PhysRevLett.71.1994.
URL <https://link.aps.org/doi/10.1103/PhysRevLett.71.1994>
- [33] C. Delfin, C. Altucci, F. D. Filippo, C. de Lisio, M. B. Gaarde, A. L’Huillier, L. Roos, C.-G. Wahlström, Influence of the medium length on high-order harmonic generation, *Journal of Physics B: Atomic,*

- Molecular and Optical Physics 32 (22) (1999) 5397. doi:10.1088/0953-4075/32/22/316.
URL <https://dx.doi.org/10.1088/0953-4075/32/22/316>
- [34] B. Henke, E. Gullikson, J. Davis, X-ray interactions: Photoabsorption, scattering, transmission, and reflection at $e = 50\text{--}30,000$ eV, $z = 1\text{--}92$, Atomic Data and Nuclear Data Tables 54 (2) (1993) 181–342. doi:<https://doi.org/10.1006/adnd.1993.1013>.
URL <https://www.sciencedirect.com/science/article/pii/S0092640X83710132>
- [35] C. Chantler, K. Olsen, R. Dragoset, J. Chang, A. Kishore, S. Kotochigova, D. Zucker, X-ray form factor, attenuation and scattering tables (version 2.1), <http://physics.nist.gov/ffast> (March 2022).
- [36] O. Smirnova, M. Ivanov, Multielectron High Harmonic Generation: Simple Man on a Complex Plane, John Wiley & Sons, Ltd, 2014, Ch. 7, pp. 201–256. arXiv:<https://onlinelibrary.wiley.com/doi/pdf/10.1002/9783527677689.ch7>, doi:<https://doi.org/10.1002/9783527677689.ch7>.
URL <https://onlinelibrary.wiley.com/doi/abs/10.1002/9783527677689.ch7>
- [37] F. Gori, G. Guattari, C. Padovani, Bessel-gauss beams, Optics Communications 64 (6) (1987) 491–495. doi:[https://doi.org/10.1016/0030-4018\(87\)90276-8](https://doi.org/10.1016/0030-4018(87)90276-8).
URL <https://www.sciencedirect.com/science/article/pii/0030401887902768>
- [38] C. Lyngå, M. B. Gaarde, C. Delfin, M. Bellini, T. W. Hänsch, A. L’Huillier, C.-G. Wahlström, Temporal coherence of high-order harmonics, Phys. Rev. A 60 (1999) 4823–4830. doi:10.1103/PhysRevA.60.4823.
URL <https://link.aps.org/doi/10.1103/PhysRevA.60.4823>
- [39] O. Hort, M. Albrecht, V. E. Nefedova, O. Finke, D. D. Mai, S. Reyné, F. Giambruno, F. Frassetto, L. Poletto, J. Andreasson, J. Gautier, S. Sebban, J. Nejdil, High-flux source of coherent xuv pulses for user applications, Opt. Express 27 (6) (2019) 8871–8883. doi:10.1364/OE.27.008871.
URL <https://opg.optica.org/oe/abstract.cfm?URI=oe-27-6-8871>
- [40] G. Russakoff, A derivation of the macroscopic maxwell equations, American Journal of Physics 38 (10) (1970) 1188–1195.

arXiv:<https://doi.org/10.1119/1.1976000>, doi:10.1119/1.1976000.
URL <https://doi.org/10.1119/1.1976000>